國立台灣大學理學院物理研究所

博士論文

Department of Physics
College of Science
National Taiwan University

Doctoral Dissertation

單分子量測系統與關聯分析之應用

Applications of Single-Molecule Spectroscopy and Correlation Analysis

楊禮綾
Li-Ling Yang

指導教授：范文祥 博士
董成淵 博士
Advisor : W.S. Fann, Ph.D
C.Y. Dong, Ph.D

中華民國 98 年 6 月
June, 2009

To my beloved family and my mentor for life

Dr. Wunshain Fann

1961 ~ 2008

~ You can have a successful career in science, academic world.
A very important thing is : Do be afraid to look like a fool. ~

中文摘要

單分子測量術近年來受到廣泛的應用，尤其在生物分子的構形、動態與其動力學的研究上。系綜測量下無法獲得的資訊，如:總體分佈及變異，則可藉由單一分子的觀察而得。本篇論文的工作旨在建立單分子光學實驗系統及方法，及其相關應用，主要涵蓋兩大部分：

1. 泛素之動態構形研究 – 單分子螢光能量移轉光譜學
2. 時間相關螢光光譜學與單光子探測技術之應用 – 共軛高分子、螢光奈米鑽石、生物分子與微流體混合器

單分子螢光能量移轉光譜學為一奈米尺度下丈量尺規，其能量移轉效率與兩標定染間的距離變化有極大的關聯。透過染料分子的標定，生物分子的構形變化與動態則會反映在螢光能量移轉效率的變化。觀測系統主要為共焦顯微鏡，根據實驗的需要將生物分子固定與玻片表面或於溶液中直接觀測。另一方面，我們亦由螢光光子資料的擷取與分析上著手，透過螢光關聯分子與光子-光子間時距的紀錄獲得額外的資訊，並成功的應用於其他相關實驗上。這些努力主要是爲蛋白質早期摺疊過程之研究而準備，希望能結合快速混合微流體元件、螢光關聯分析與螢光能量移轉光譜以解析摺疊動態。

Abstract

Single-molecule detections have been known for the potential to provide additional information beside ensemble measurements. Population heterogeneities and synchronous (or asynchronous) reaction pathways pertaining to conformational dynamics and molecular interactions are veiled by ensemble averaging. The scope of this thesis is to establish general experimental methodologies on the basis of single-molecule detection, and the applications have been covered as well. The frame of this work is mainly composed of two parts:

1. Conformational dynamics of ubiquitin are investigated by spFRET (single-paired Förster Resonance Energy Transfer).
2. Applications of TCSPC (Time-Correlated Single Photon Counting) and FCS (Fluorescence Correlation Spectroscopy) on conjugated polymers, FND (Fluorescence Nano Diamond), biomolecules and micro-fluidics.

FRET serves as a distance ruler in close proximity (~ 1 nm to ~ 10 nm), and dynamic changes in structure of proteins can be thus recorded accurately. We have established optical methods to observe ubiquitin molecules either immobilized on the cover-slip surface or in free solution. On the other hand, detections based on single photon counting and correlation analysis has also been applied for further information aside from intensity analysis. At the same time, a continuous-flow micro-fluidic mixer is under development, which has claimed sub-ms mixing dead time. Cooperating FCS, TCSPC, microscopy, micro-fluidic mixer and FRET provides us with the perspective on investigations population evolution and structural variations in along the kinetics of biomolecules.

Table of Contents

Lists of Figures

CHAPTER 1

INTRODUCTION

1.1: Overview on Thesis

This thesis is mainly composed of five parts. A brief introduction to the development of single-molecule detection is in the first chapter. In chapter 2, the principle of confocal microscopy and förster resonance energy transfer (FRET), and the basic of fluorescence correlation spectroscopy (FCS) are covered. Applications of FCS and analysis programming based on TCSPC (time-correlated single photon counting) are summarized in chapter 3. Results and discussions over our observations on ubiquitin by spFRET (single-pair FRET) are in chapter 4. Concluding remarks and the perspective regarding applications of spFRET, correlation analysis and single-photon counting technique concluded in the final chapter.

1.2: Development of Single Molecule Spectroscopy

The first single molecule detection (SMD) was realized by Moerner et al in 1989 [1], and single molecule spectroscopy (SMS) has become more and more popular in the following 15 years. A number of articles and books address the different aspects of single-molecule investigations on fluorescent objects from nano-crystals to biomolecules[2, 3]. On the other hand, the techniques and methods evolve rapidly to gain better signal-to-noise ratio (S/N ratio) and longer observation time. The wide applications of SMD (single-molecule detection) on the study of conformation of biomolecules provide new insights into the shadowy relations behind functions and structures. The rotational motions of F1-ATPase was directly observed by the group of Yanagida in 2000 [4]. The combination of confocal microscopy with förster resonance energy transfer (FRET), which serves as a distance ruler at nano-meter scale, opens up the gate between physics and bio-chemistry. The conformational switch of the activate single RNA ribozyme molecule between docked and undocked state in the presence of substrate was firstly observed by T. Ha and Zhuang et al [5, 6].

At the same time, the analysis on fluorescence not only addressed the emission intensity but was push into the regime of correlation and single-photon counting [3, 7-9]. Fluorescence emission is generated by spontaneous emission from the electronic excited state with a lifetime of nanosecond [9]. It is a slow process comparing with other non-radiative relaxations (intersystem crossing, radical-ion state for quantum dots, and quenchers), which leads to the loss of fluorescence. Furthermore, all the factors would contribute to the detected fluorescence intensity, and interfere with the process in study (such as förster resonance energy transfer). For example, widespread fluorescence intermittency (blinking or flickering) is though the hallmark of single-molecule signals; its interference with the signature of conformational dynamics obscures the observation. Though complexities of photo-physical or photo-chemical properties of dyes limit the development of SMD, the origins of fluorescence intensity fluctuations could be discerned with the help of fluorescence correlation analysis.

We are inspired to combine SMD with fluorescence techniques in order to gain better understanding of structural dynamics of biomolecules at the molecular level. Furthermore, our long-term objective is to study the folding kinetics at single-molecule level such that the evolution of the distribution of conformers along the folding path could be determined. Förster resonance energy transfer (FRET) and correlation analysis are adopted in view of the conformational dynamics of proteins and the complexity of fluorescence intensity of dye molecules.

CHAPTER 2

EXPERIMENTAL METHODS & APPARATUS

To achieve single-molecule detection (SMD), lowering the background noise and high sensitivity detectors are both critical. There are two approaches to realize single-molecule observations in general. One is total internal reflection microscopy (TIRF); the other is confocal microscopy. In TIRF one can easily acquire an image in an area of ~ 100 μm x 100 μm, and the best time resolution so far is 1 ms, limited by the photon flux of dyes. Since the excitation is through the evanescent electric field which dissipates within 100 nm, the scattered light from the solution is negligible and background noise can be lowered. The advent of EM gain CCD, which has the sensitivity to a single dye molecule, opens the gate of the applications of TIRF on single-molecule detection. On the other hand, confocal microscopy is the other option for low signal detection because of the tight focus to optical diffraction limit. With the introduction of the second pinhole in front of detectors, the scattered light can be greatly reduced. The advantages of confocal microscope are its capability of 3D imaging, the tunable time resolution on single photon counting base, and compatibility with lifetime/fast correlation measurement.

2.1: Confocal Microscopy

"Confocal" refers to that an object and its corresponding image shares the same focus. That is, the image has the same focus as the point of focus in the object. The main advantages of confocal microscopy are the elimination of out-of-focus glare and the shallow depth of field compared with the conventional bright wide-field imaging microscopy. Theses offer the ability of serial sections of thick specimens and high signal-to-noise ratio. Figure 1 is the optical pathway inside the confocal microscope [10], which shows that the introduction of the pinhole aperture can block the stray light and the emission out of focus plane. The excitation light is only condensed by the objective and focused onto the sample plane to diffraction limit. The size of the pinhole aperture in front of detectors is crucial for the determination of the final image focal spot, especially in the axial direction.

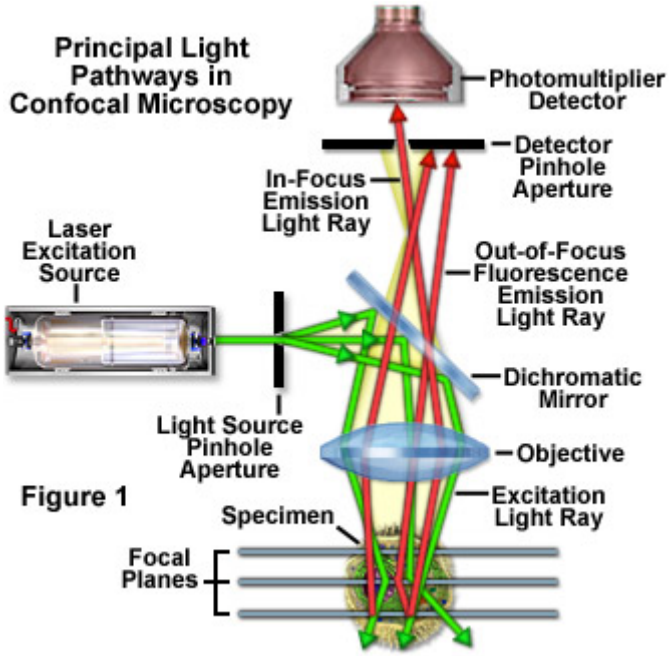

Figure 1. Optical pathway in confocal microscope [11].

There are two branches of scanning modes for confocal microscope. One is laser-scanning (mirror-scanning); the other is stage-scanning (sample-scanning). Our home-built confocal system adopts the stage-scanning mode for its precise and reliable positioning ability. The trade-off of the stage-scanning system is the slow imaging rate. Generally, it takes 3 – 4 minutes for 20 μm x 20 μm image for single chromophore imaging in our home-built confocal microscope. The optical path is illustrated in Figure 1. The confocal microscope shares the same framework as the epi-fluorescence microscopy except for the size of the excitation area on the sample plate. The excitation and emission light is condensed and collected by the same objective, and a dichroic mirror which reflects excitation is introduced into the optical path to increase the contrast. Confocal microscopy offers several advantages over the conventional optical microscopy, such as shallow depth of field (Figure 2), reduction of out-of-focus light, and optically sectioning ability. This optically sectioning ability makes confocal microscope gain a great population in the field of bio-imagining.

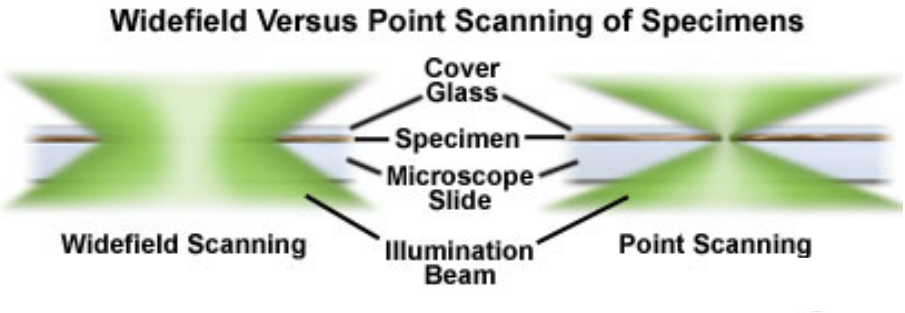

Figure 2. Depth of field of conventional optical microscope and confocal microscope [12].

The spatial resolution of confocal microscope is limited by the Airy diffraction pattern which corresponds to a point light source. The image of the sample is constructed by a series of closely spaced point light sources. Numerical aperture of an objective not only determines the magnifying power but also affects the spatial resolution. The higher the numerical aperture, the better the spatial resolution. The wavelength of light is also a determining factor of the resolution, Equation (1).

$$\Delta r = \frac{1.22\ \lambda}{2N.A.} \tag{1}$$

For a 100 X oil immersion objective at 500 nm, the spatial resolution is around 0.23 μm ideally. However, the optical alignment will also affect the spatial resolution. The light cone and size of excitation laser are critical and should be matched to the objective.

2.2: Förster Resonance Energy Transfer (FRET)

Förster resonance energy transfer (FRET) proposed by T. Förster in 1948 [13] is the energy transfer mechanism between a pair of dye molecules, donor and acceptor, through dipole-dipole interactions, Figure 3. The energy of donor in electronic excited state could be transferred non-radiatively to the acceptor such that it becomes excited instead. The energy transfer efficiency is strongly dependent on the distance between the pair of chromophores (Equation (3)), which makes FRET a popular technique in the study of interactions and conformational dynamics of biomolecules [14, 15]. As a spectral ruler at

nm scale, the sensitive regime of a dye pair is determined by the emission spectrum of donor and absorption spectrum of acceptor, Equation (2) [16]. The förster radius, R_0, serves as a measure to the sensitive regime of the chosen dye pair, which is defined as the distance as the energy transfer efficiency equals to 50%. In addition to the degree of spectrum overlap, the index of refraction in Equation (2) can seriously affect R_0 for the exponent of being "4". The förster radius, R_0, can varies from 60 Å at n = 1.0 to 50.3 Å at n = 1.3. The other important factor is the relative flexibility of dipole orientations of the FRET pair. The effect of dipole orientations has been taken into account in terms of κ^2 in Equation (2). The coefficient,κ^2, is equivalent to 2/3 for freely rotating donor and acceptor dipoles.

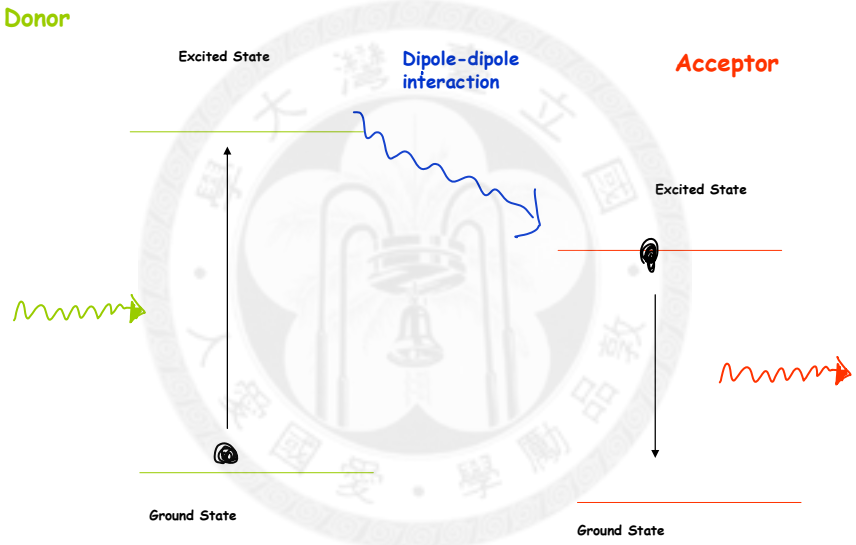

Figure 3. Schematic illustration of FRET process

$$R_0 = [8.8\times10^{23}\cdot\kappa^2\cdot n^{-4}\cdot QY_D\cdot J(\lambda)]^{\frac{1}{6}}\ \text{Å}$$

κ^2 : diople orientation factor $(0\sim4)$

$(\kappa^2 = \frac{2}{3}$ for randomly oriented donors and acceptors)

QY_D : fouorescence quantum yield of the donor in the absence of the acceptor

n : index of refraction

$J(\lambda)$: spectral overlap integral

(2)

Practically, FRET efficiency can be determined by either the intensity of donor and acceptor or the lifetime change of donor in the presence and in absence of acceptor. The relation among FRET efficiency (E), intensity (I_D, I_{DA}) and lifetime (τ_D,τ_{DA}) is shown in Equation (3). The energy transferring caused by dipole-dipole interactions can be deduced from quantum mechanics. The derivation of FRET efficiency is included in the sub-section 2.2.1.

$$E = \frac{1}{1+(\frac{r}{R_0})^6} = 1-\frac{I_{DA}}{I_D} = 1-\frac{\tau_{DA}}{\tau_D}$$

I_D : fluorescence intensity of donor in absence of acceptor

I_{DA} : flrescence intensity of donor in the presence of acceptor

τ_D : donor lifetime in absence of acceptor

τ_{DA} : donor lifetime in the presence of acceptor

(3)

2.2.1: Derivation of FRET Efficiency

Consider that the donor is initially populated in electronic excited state while the acceptor is in ground state as shown in Equation (4). The energy of donor is transferred to the acceptor via dipole-dipole interactions and the rate is defined as κ_{FRET}. We start from Fermi's golden rule, and the transition rate, κ_{FRET}, can be written into Equation (5). The energy between two brackets is the energy of acceptor dipole moment in the potential generated by donor dipole moment.

$$D_{excited} + A_{ground} \xrightarrow[\kappa_{FRET}]{} D_{ground} + A_{excited} \tag{4}$$

$$\kappa_{FRET} \propto \left| \left\langle \varphi_{D_{ground}} \varphi_{A_{excited}} \left| \frac{\alpha_f \mu_D \mu_A}{r^3} \right| \varphi_{D_{excited}} \varphi_{A_{ground}} \right\rangle \right|^2 \tag{5}$$

Since the coordinates of donor and acceptor are independent, the two dipole moments can be further separated in Equation (5) and then reduced (Equation (6)). The former term is in the same form as transition of donor emission; the latter one is that of acceptor absorption.

$$\kappa_{FRET} \propto \frac{\alpha^2}{r^6} \left| \left\langle \varphi_{D_{ground}} \varphi_{A_{excited}} \left| \mu_D \right| \varphi_{D_{excited}} \varphi_{A_{ground}} \right\rangle \right|^2 \left| \left\langle \varphi_{D_{ground}} \varphi_{A_{excited}} \left| \mu_A \right| \varphi_{D_{excited}} \varphi_{A_{ground}} \right\rangle \right|^2 \tag{6}$$

According to Einstein's coefficients derived in the optical process, FRET transferring rate is related to quantum efficiency, lifetime of donor and absorption coefficient of acceptor. By generalizing it into a function of frequency, the primary relationship between spectral integral and FRET transferring efficiency is obtained, Equation (7). R_0 is defined by the spectral integral, Equation (8); α is the coefficient including the effects of index of refraction and relative dipole orientations. The final form of förster radius, R_0, is shown in Equation (9). J(λ) is the spectral integral in terms of wavelength, and the unit is cm^3M^{-1}.

$$\kappa_{FRET} \propto \frac{1}{r^6} \cdot \frac{\phi_D}{\tau_D} \cdot \int \varepsilon_A(\nu) \cdot f_D(\nu) \cdot \nu^{-4} d\nu \tag{7}$$

$$R_0 \equiv \alpha \cdot [\int \phi_D \cdot \varepsilon_A(\nu) \cdot f_D(\nu) \cdot \nu^{-4} d\nu]^{\frac{1}{6}} \tag{8}$$

$$R_0 = [8.8 \times 10^{23} \cdot \kappa^2 \cdot n^{-4} \cdot \phi_D \cdot J(\lambda)]^{\frac{1}{6}} \text{ Å}$$

(9)

Whereas,

$$\kappa_{FRET} = \frac{1}{\tau_D} \cdot (\frac{R_0}{r})^6$$

(10)

And,

$$E \equiv \frac{\kappa_{FRET}}{\frac{1}{\tau_D} + \kappa_{FRET}}$$

(11)

Substituting Equation (10) into Equation (11), we can obtain Equation (3), which we are more familiar with.

2.3: Fluorescence Correlation Spectroscopy (FCS)

Correlation analysis is firstly proposed by Wiener in 1949 [17], and its application in fluorescence was realized in 1970s [18-20]. In fluorescence correlation spectroscopy (FCS), the intensity fluctuation is analyzed, which is generally overwhelmed in ensemble measurements due to the great amount of molecules involved. With the decrease of concentration (nM ~ pM), the intensity fluctuation becomes more prominent such that the information behind the seemingly random and meaningless signals can be extracted. The sources resulted into the observed fluorescence intensity fluctuation can be concentration variations, photophysical process of the chromophore itself [21] or fluctuation of any other factor pertinent to fluorescence. However, the low signal-to-noise ratio in detection of few molecules at a time limited the application of FCS until its combination with confocal microscopy by Rigler et al [21-23]. The drastic shrinkage of detection volume in confocal microscopy leads to the breakthrough in the application of FCS. On the one hand, the signal-to-noise ratio is boosted due to the great reduction of out-of-focus excitation

scattered light. On the other hand, the contrast of correlation is raised since the intensity fluctuation is amplified by limiting the number of detected molecules. The general form of the intensity correlation function reads as follows:

$$G^{(2)}(\tau) \equiv \frac{\langle I(t)\cdot I(t+\tau)\rangle}{\langle I(t)\rangle^2} = 1+\frac{\langle \delta I(t)\cdot \delta I(t+\tau)\rangle}{\langle I(t)\rangle^2} = 1+g^{(2)}(\tau)$$

$$\delta I(t) = I(t)-\langle I(t)\rangle; \langle I(t)\rangle = \frac{1}{T}\int_0^T I(t)dt \tag{12}$$

The capital $G^{(2)}(\tau)$ is defined as the autocorrelation function of detected fluorescence intensity while the $g^{(2)}(\tau)$ is that of fluorescence intensity fluctuations. Concentration variations, photophysical process or any other physical/chemical reaction which can lead to fluorescence intensity change with time will contribute to the measured FCS curves. In the following sub-sections, we are going to summarize few different cases for FCS.

2.3.1: Basics of Correlation Function

At room temperature, the fluorescent emission of a single chromophore after being excited is incoherent [24]. Therefore, the fluorescence can be regarded as an incoherent superposition of fields of many sources, and adding up the intensities of all sources leads to the final total intensity one can detect. The superposition of all incoherent fields is in the mathematic form shown in Equation (13). That is, superimposing many fields of different emitting sources with random phases (φ_i); that each source has the same field and different phases is assumed. The first-order correlation function, $G^{(1)}(\tau)$, is derived from the correlation of electric fields, Equation (14).

$$\vec{E} = i\sum_i e^{i\varphi_i}\cdot\vec{E_0}(t-t_i) \tag{13}$$

$$G^{(1)}(\tau) \equiv \frac{\langle E(t+\tau)\cdot E'(t)\rangle}{\langle E^2(t)\rangle} = \frac{\langle E_0(t+\tau)\cdot E_0'(t)\rangle}{\langle E_0^2(t)\rangle}$$

(14)

The auto-correlation function of fluorescence intensity, $G^{(2)}(\tau)$, people are familiar with is the second-order correlation function, Equation (15). The relation between first-order and second-order correlation function of fluorescence has been described in Equation (16).

$$G^{(2)}(\tau) = \frac{\langle I(t+\tau)\cdot I(t)\rangle}{\langle I(t)\rangle^2}$$

(15)

And,

$$G^{(2)}(\tau) = 1 + \left\{G^{(1)}(\tau)\right\}^2$$

(16)

The physical picture of correlation of fluorescence intensity can be simply depicted in Figure 4. The recorded intensity variation with time, I (t), is duplicated, delayed by a period of time, τ, and multiplied to the original I (t). The left-hand-sided panel shows us the typical correlation function versus delay time.

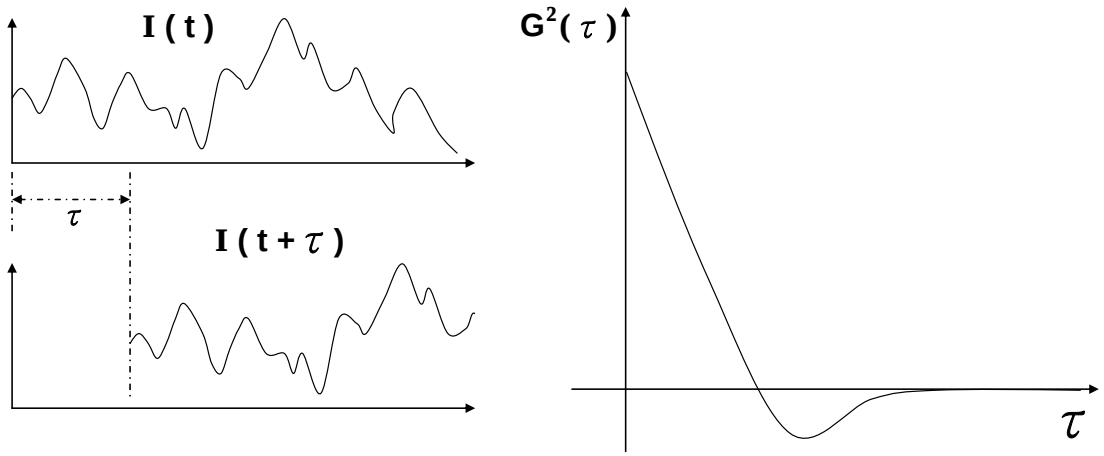

Figure 4. Schematic drawing of auto-correlation of optical intensity.

The main feature of the intensity autocorrelation function is a plateau at certain meaningful delay time. The autocorrelation function is sensitive to the fluctuating signals; specific time scales corresponding to sources leading to signal variations with time can be projected, which has been illustrated in Figure 5. The reddish cone in panel (A), Figure 5 is defined by the collimated excitation laser, and corresponds to the focal volume as Equation (27) shows, which will be discussed later on. Movements of fluorescent particles (translational and rotational), inter-system crossing (photophysical process) or additional chemical reactions are all the possible sources. A concrete idea on the development of the autocorrelation curves is demonstrated in panel (B),Figure 5. Imagine that a fluorescent particle is swimming through the excitation focal volume, and the corresponding variation of fluorescent emission with time can be recorded precisely. Then, what we should observe is a perfect Gaussian intensity profile convoluted with some noise (shot noise). The value of correlation is maximized at $\tau = 0$, and approaching zero as the delay time, τ, is larger than the average diffusing time of the fluorescent particle through the excitation cone. In the middle of the two extremes, correlation is decreasing with the delay time.

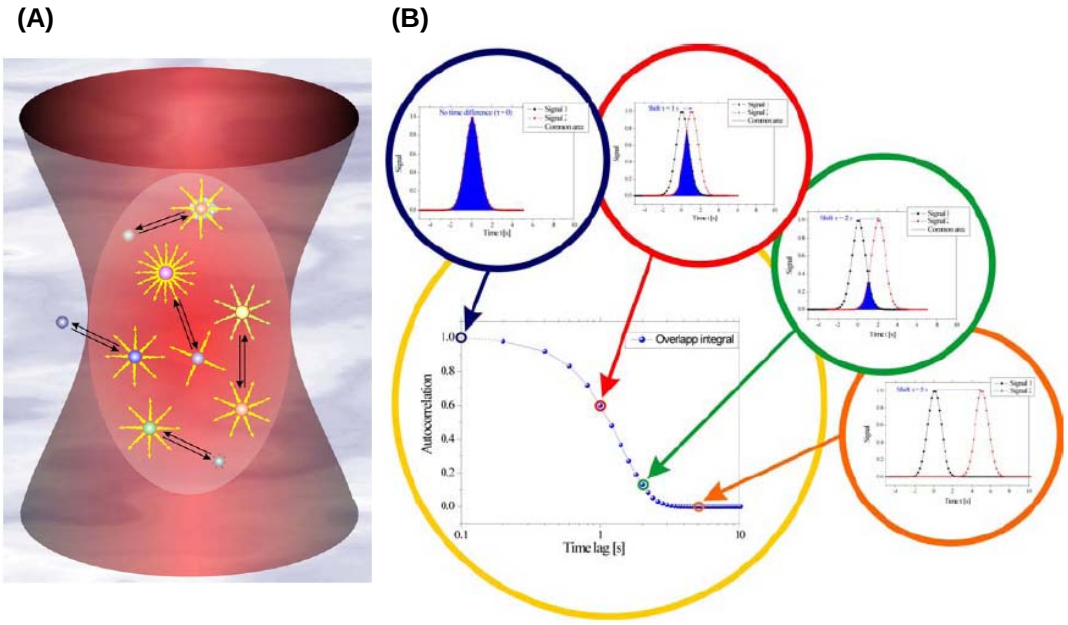

Figure 5. (A) Molecular mechanisms that might lead to fluorescence fluctuations comprise particle movements, conformational changes, chemical or photophysical reactions. (B) Development of the auto-correlation function [25].

Figure 6 is what one should be able to observe in the autocorrelation of fluorescence emission for freely diffusing fluorescent objects if super-short time resolution is achieved (~ ps) and limitations of instruments have been neglected. Generally, the slowest process is translational diffusion (~ ms), and the time scale of rotational motion is around few tens of ns. Another typical photophysical process relating to phosphorescence originates from the inter-system crossing from excited singlet sate to the triplet state. Typically, the inter-system crossing has the time scale in the range from few tenths of μs to ms, and is strongly dependent on the environments. So far, the mentioned processes are still in the regime of classical optics; the quantum phenomena (antibunching) could be observed as the time resolution goes down to ps, that is, the property of photons [7, 9, 26, 27].

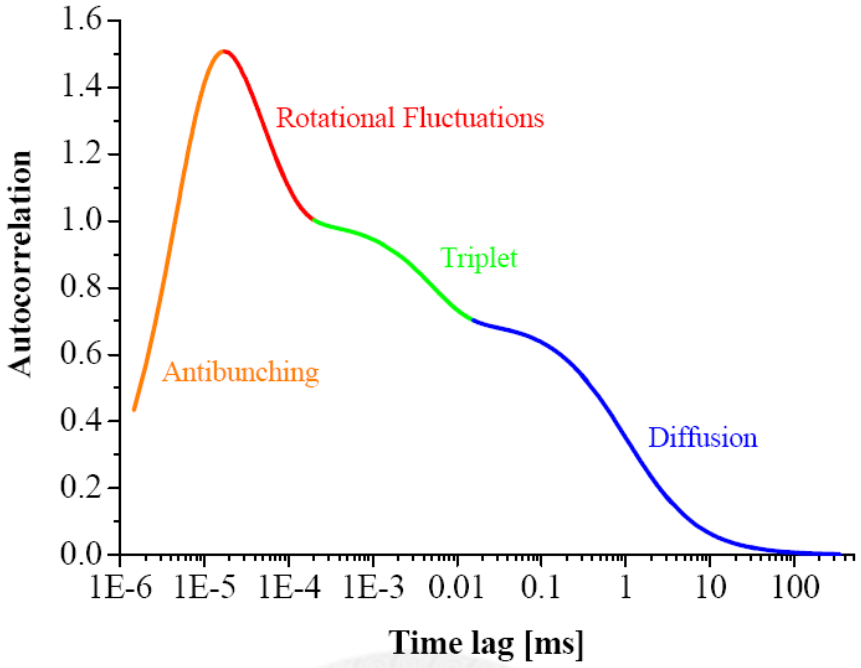

Figure 6. Time scales of various processes investigated by fluorescence autocorrelation spectroscopy [28].

Consider that one chromophore is excited and emitting photons, and a 50/50 beam splitter is introduced such that the photon stream is divided into two branches and collected by detectors respectively. From the perspective of quantum optics, an incoming photon encountering the beam splitter could choose either one route or the other, and the probability of each route is 50%. Therefore, it could never be possible for two detector seeing photons at the same time, which leads to observed "antibunching". As the dip at $\tau = 0$ approaches zero, it implies one chromophore emitting photons at a time.

The processes above will be discussed into detail in the following sub-sections, including the equivalence between correlation and the arrival-time distribution between photons [7, 9, 27, 29, 30].

Background Issues on FCS

In reality, a constant or uncorrelated background, "B", is always accompanying measurements, and it will reduce the contrast of the real correlation function, $G^{(2)}_{real}(\tau)$. The relation between measured autocorrelation of fluorescence, $G^{(2)}_{exp}(\tau)$, and the real one, $G^{(2)}_{real}(\tau)$, is listed in Equation (18).

$$G_{real}^{(2)}(\tau) = \frac{1}{\rho^2} \cdot [G_{\exp}^{(2)}(\tau) - (1-\rho^2)] \;;\; \rho \equiv \frac{< I(t) >}{< I(t) > + B}$$

(17)

$$g_{\exp}^{(2)}(\tau) = G_{\exp}^{(2)}(\tau) - 1 = \rho^2 \cdot (G_{real}^{(2)}(\tau) - 1)$$
$$= (1 + \frac{B}{< I(t) >})^{-2} \cdot g_{real}^{(2)}(\tau)$$

(18)

The autocorrelation of intensity fluctuations can be further derived as Equation (18) shows. According to Equation (18), $g^{(2)}_{real}(\tau)$ is approaching $g^{(2)}_{exp}(\tau)$ as B << <I(t)>, and $g^{(2)}_{real}(\tau)$ is always larger than $g^{(2)}_{exp}(\tau)$ since ρ is less than 1 in real world. That is, the existence of background either constant or random will lead to overestimation of average particle numbers in focal volume (diffusion) or underestimation of the amplitude corresponding to processes in study.

2.3.2: Derivation of 3D diffusion

Consider that the incident excitation laser beam is condensed by an objective and the intensity profile reads as follows:

$$P(r) = e^{-2\frac{x^2+y^2}{r_0^2}} \cdot e^{-2\frac{z^2}{z_0^2}}$$

(19)

Since fluorescent particles are swimming in and out of the excitation focal volume continuously, the recorded fluorescence intensity fluctuates with time.

$$\delta I(t) = \int_V P(r) \cdot \delta(\eta \cdot C(r,t)) \cdot dV$$

(20)

Here, η is determined by the quantum yield, the absorption cross-section, and the excitation power. C(r,t) is the concentration function of fluorescence particles in solution. The autocorrelation function can be written into the following form.

$$g^{(2)}(\tau)=\frac{\langle \delta I(t)\cdot \delta I(t+\tau)\rangle}{\langle I(t)\rangle^{2}}$$
$$=\frac{\iint P(r)\cdot P(r')\langle \delta(\eta\cdot C(r,t))\delta(\eta\cdot C(r',t+\tau))\rangle dV dV'}{(\int P(r)\cdot\langle \delta(\eta\cdot C(r,t))\rangle dV)^{2}} \tag{21}$$

While,

$$\delta(\eta\cdot C(r,t))=C(r,t)\cdot\delta\eta+\eta\cdot\delta C(r,t) \tag{22}$$

Assume that the fluorescent properties are not changing within the observation time, and the first term in Equation (22) can be neglected. We have to take care of the second term only in Equation (22) in the autocorrelation analysis, and the equation can be further simplified into Equation (23).

$$g^{(2)}(\tau)=\frac{\iint P(r)\cdot P(r')\langle \delta C(r,0)\delta C(r',\tau)\rangle dV dV'}{(\langle C\rangle\cdot\int P(r)\cdot dV)^{2}} \tag{23}$$

where,

$$\langle \delta C(r,0)\delta C(r',\tau)\rangle=\langle C\rangle\cdot\frac{1}{(4\pi D\tau)^{\frac{3}{2}}}\cdot e^{-\frac{(r-r')^{2}}{4D\varsigma}} \tag{24}$$

such that,

$$g^{(2)}(\tau)=\frac{1}{\langle C\rangle(4\pi D\tau)^{-\frac{3}{2}}}\cdot\frac{\iint P(r)\cdot P(r')\cdot e^{-\frac{(r-r')^2}{4D\tau}}dVdV'}{\left(\int P(r)dV\right)^2} \tag{25}$$

Since,

$$\tau_D\equiv\frac{r_0^2}{4\cdot D} \tag{26}$$

And, the definition of the effective excitation focal volume reads as follows;

$$\mathrm{V_{eff}}\equiv\frac{(\int P(r)dV)^2}{\int P^2(r)dV}=\frac{(\int e^{-2\frac{x^2+y^2}{r_0^2}}\cdot e^{-2\frac{z^2}{z_0^2}}dV)^2}{\int e^{-2\frac{x^2+y^2}{r_0^2}}\cdot e^{-2\frac{z^2}{z_0^2}}dV}=\pi\cdot r_0^2\cdot z_0 \tag{27}$$

$$g^{(2)}(\tau)=G^2(\tau)-1=\frac{1}{V_{eff}\cdot<C>}\cdot\frac{1}{\left(1+\frac{\tau}{\tau_D}\right)}\cdot\frac{1}{\sqrt{1+\left(\frac{r_0^2}{z_0}\right)^2\cdot\left(\frac{\tau}{\tau_D}\right)}} \tag{28}$$

Determination of Flow Rate

The fluorescence intensity autocorrelation function can be further modified in the case of flow, Equation (29) [31].

$$g^{(2)}(\tau)=\frac{1}{V_{eff}\cdot\langle C\rangle}\cdot\frac{1}{\left(1+\frac{\tau}{\tau_D}\right)}\cdot\frac{1}{\sqrt{1+(\frac{r_0}{z_0})^2\cdot(\frac{\tau}{\tau_D})}}\cdot\exp\left\{-(\frac{\tau}{\tau_{flow}})^2\cdot\left(1+\frac{\tau}{\tau_D}\right)^{-1}\cdot\left(1+\left(\frac{r_0}{z_0}\right)^2\cdot\frac{\tau}{\tau_D}\right)^{-\frac{1}{2}}\right. \tag{29}$$

As the flow velocity is fast enough to dominate translational motions, i.e.

$$\tau_{flow} << \tau_D \tag{30}$$

Equation (29) can be further approximated into the following form.

$$g^{(2)}(\tau) = \frac{1}{V_{eff} \cdot \langle C \rangle} \cdot \exp(-\frac{\tau}{\tau_{flow}}) \tag{31}$$

2.3.3: Bunching and Antibunching

Bunching Effect of Triplet State

There is generally a triplet state existing between its singlet excited state and ground state for organic molecules. The transition between the singlet excited state and triplet state is via weak spin-orbit coupling and termed as "Inter-System Crossing (κ_{ISC})". The lifetime of the excited electron is at the time scale of ms or even longer, and this radiative relaxation process generally gives rise to phosphorescence (κ_{ph}), Figure 7. The existence of triplet state often accelerates photo-bleaching of organic dyes, and leads to intermittence (on-off blinking) behaviour for single-molecule studies.

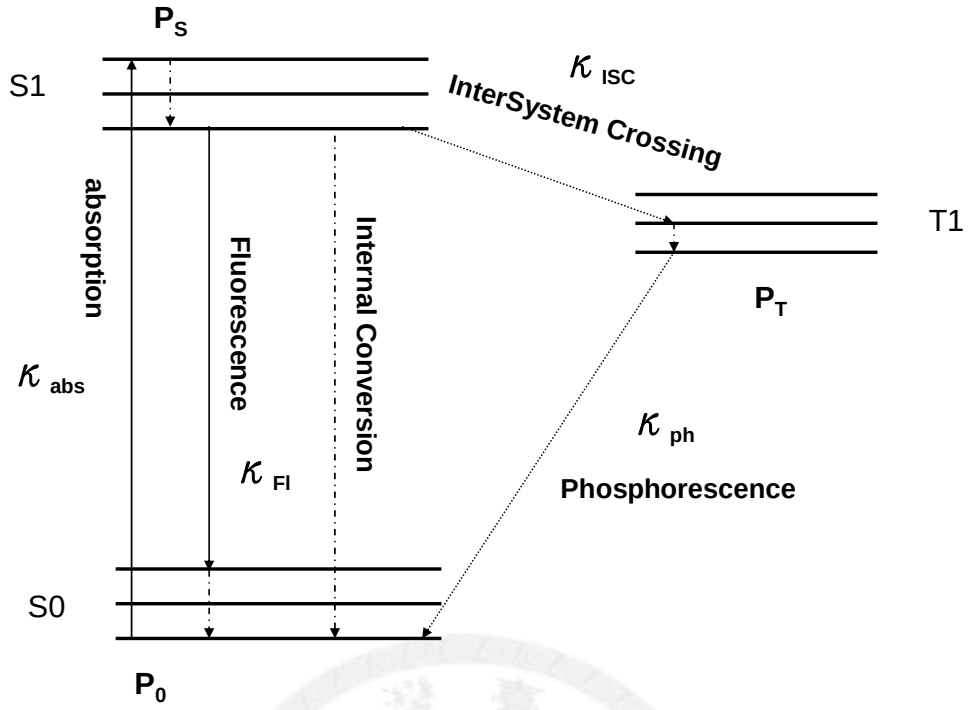

Figure 7. Jocobian diagram.

For autocorrelation of fluorescence intensity, this intersystem crossing results into the bunching effect following the anti-bunching dip [32]. Assume that the population density in ground state is P_0 and population densities in singlet excited and triplet state are P_S and P_T respectively. The absorption, fluorescence, intersystem-crossing and phosphorescence rate are termed as κ_{abs}, κ_{FI}, κ_{ISC} and κ_{ph} individually, Figure 7. In equilibrium, the population densities of the three states are dependent on one another, Equation (32).

$$P_0 = \frac{\kappa_{FI}}{\kappa_{FI} + \kappa_{abs}} \cdot (1 - P_T) \;;\; P_S = \frac{\kappa_{abx}}{\kappa_{FI} + \kappa_{abs}} \cdot (1 - P_T) \tag{32}$$

The solution to the rate equation of this three-level system is described by Equation (33) (stimulated emission is assumed absent in low excitation rate). The convolution of exponential function still takes the same mathematical form, Equation (34), but the prefactor varies.

$$P_S = a + b \cdot e^{-\lambda t} \;\; ; \;\; \lambda = \kappa_{ph} + \frac{\kappa_{abs} \cdot \kappa_{ISC}}{\kappa_{FI} + \kappa_{abs}} \tag{33}$$

$$G^2(\tau) = 1 + c \cdot e^{-\lambda t} \;\; ; \;\; c = \frac{\kappa_{abx} \cdot \kappa_{ISC}}{\kappa_{ph} \cdot (\kappa_{FI} + \kappa_{abs})} \tag{34}$$

The picture concerning the bunching effect is quite straightforward. In the beginning, the molecule is emitting photons at a higher rate, but trapping by the triplet state in the following makes it silent on the order of its triplet lifetime (~ μs – ms). After the molecule return to its ground state, it becomes active and capable of emitting light again until the next trapping [7, 9]. Discussions above stay in the regime of low excitation rate. The discussion over intensity autocorrelation analysis at high excitation rate (sufficient to initiate stimulated emission) is beyond the scope of the discussion in this chapter.

Anti-bunching of Single Fluorescent Object

To study reactions occurring at shorter time scale (below μs), artefacts from detectors should be taken into account. Real detectors suffer from dead time limitations and afterpulsing effects. Dead time is defined as a period of time in which a detector is "blind" after detecting an event. In other words, a detector could not receive two events whose spacing is shorter than its dead time. Take avalanche photodiode (APD) as an example, its dead time is around 100 ns. Therefore, if only one detector is in use for autocorrelation analysis, it could never be possible to have the shortest time scale go below its dead time.

2.3.4: Other Sources of Fluorescence Fluctuations

In addition to the triplet state of molecules, there are still some other sources which might give rise to bunching effect [7, 9]. The first one is often seen at low temperature [33], and it is attributed to the sharp absorption lineshape and excitation with a narrow-banded laser. Variations in the absorption spectrum of the molecule could lead to intensity fluctuations since the molecule might be out of the excitation resonance from time to time. Beside the translational diffusion into and out of excitation focus, the rotational diffusion of the dipole

moment with respect to the polarization of excitation will also come into play [34]. “Blinking” is an important feature of immobilized single molecule behaviour. However, its origins are still not clear and quite complicated [35]. For organic dyes, the origin of on-off blinking is generally attributed to the triplet state. Nevertheless, there are still some other factors could dominate the shorter time scale blinking behaviour, especially the addition of a variety of chemicals to prevent photobleaching [36-38]. The source of the blinking behaviour of quantum dots is quite different from that of organic dyes. Since the electron is created by excitation in the outer shell of a quantum dot, the loss of that electron will prevent the electron-hole from recombining such that the quantum dot is like being trapped in a dark state. Photobleaching is the last source people would like to see in the autocorrelation experiment for its confusion with other sources in study.

CHAPTER 3

APPLICATIONS OF CORRELATION ANALYSIS

The results and discussions in chapter 3 are based on fluorescence intensity analysis. Nevertheless, a lot of factors could bias the results of intensity analysis, such as scattered light and background photons [39]. Correlation analysis on the intensity which is sensitive to the signal variations could assist in clarifying the origins of fluorescence fluctuations. On the other hand, time correlated single photon counting (TCSPC), which records the time difference of each pair of detected photons or arrival time of a photon relative to the trigger precisely, provides us with further information pertinent to either fluorescence lifetime or correlation analysis at short time scale (< 1 μsec). In this chapter, our efforts on FCS and TCSPC and their applications are summarized.

3.1: Size Characterization of Fluorescence NanoDiamond (FND)

The negatively charged nitrogen-vacancy defect center, $(N\text{-}V)^-$, in type Ib diamond is a robust fluorescent nano-object which has ultrahigh photo-stability (neither photobleaching nor blinking), and has drawn much attention in recent years [40]. These desirable optical properties, along with its non-toxic nature, have made FND a promising candidate for the applications of bio-imaging [41-43]. Despite the unique photophysical properties of FNDs, the size of this nano-object is an important parameter to characterize since the size-controlled production is not yet well developed. Measurements of FCS on FNDs in free solution can provide the information concerning the average size [44, 45].

$$\tau_D = \frac{r_0^{\,2}}{4D} \;;\; D(R6G) = 0.28\ \mu m^2 / m\,\text{sec} \tag{35}$$

The effective focal volume of the confocal microscope was characterized by the organic dyes, R6G, in advance. Since the diffusivity (diffusion coefficient) of R6G is known (0.28 μm^2/msec), the effective focal volume can be obtained by fitting to the 3D-diffusion model, Equation (28). The calibrated dimension of the excitation focal volume is 0.34 μm in r_0 (radial) and 0.85 μm in z_o (axial), which corresponds to ~ 0.54 *fl*. How the size of

diffusing particles affects the fluorescence autocorrelation curves is illustrated in Figure 8. Fluorescence microspheres with different diameters (60 nm and 120 nm) are measured and compared with R6G. The fluorescence autocorrelation curve shifts to the longer time scale (right-handed side) as the particle size increases.

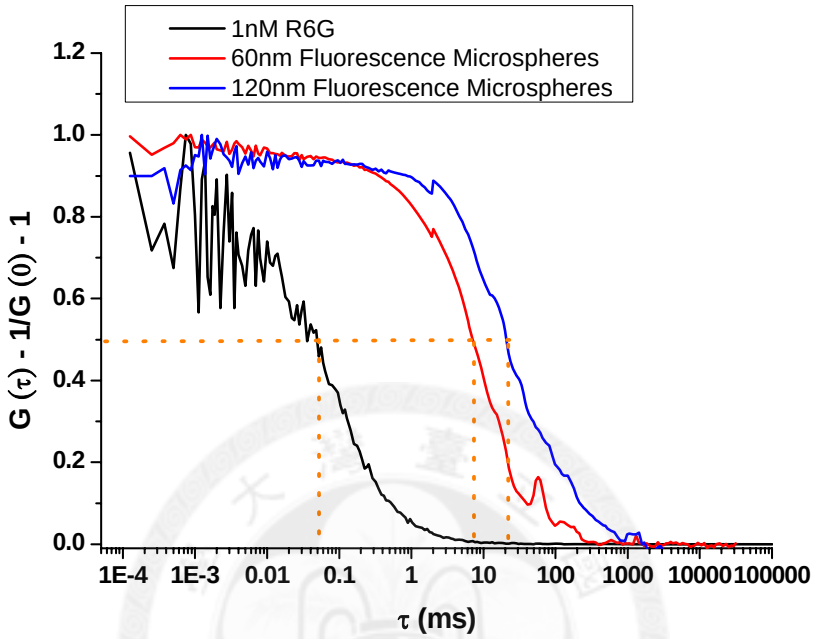

Figure 8. Normalized auto-correlation curves of organic dyes (R6G), 60 nm and 120 nm fluorescence microspheres. The effective focal volume of the confocal microscope is characterized by the organic dyes, R6G, and its diffusion coefficient is 0.28 μm^2/msec.

Three different sized FNDs (10 nm, 35 nm and 100 nm) in free solution are measured, Figure 9. Fluorescence microspheres (60 nm and 120 nm) serves as references, and the shape effects are neglected [46].

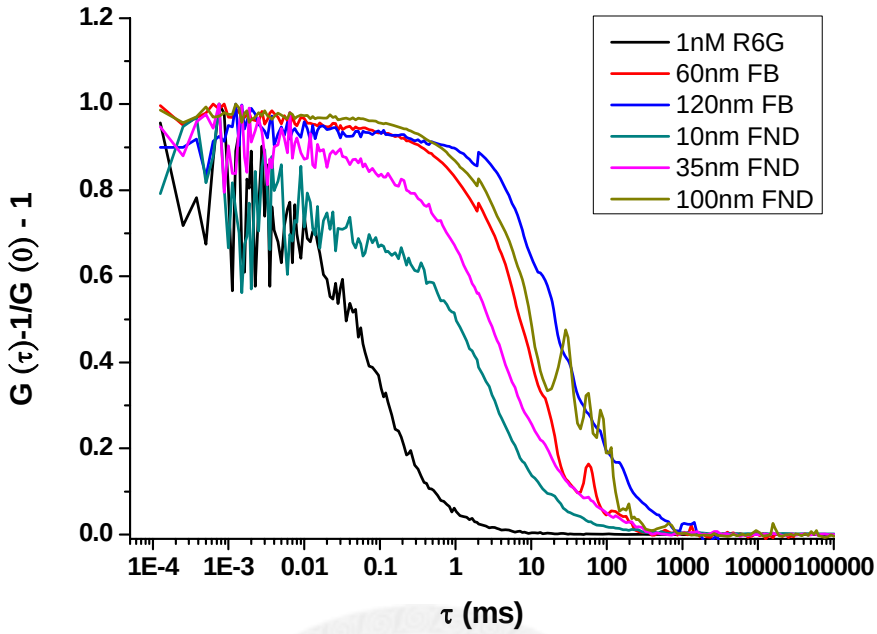

Figure 9. Comparison of the autocorrelation curves of different-sized FNDs and fluorescence micro-spheres in FCS

3.2: Determination of Flow velocity of Microfluidic Mixer

The advantage of micro-fluidic mixer based on "hydrodynamic focusing" is the potential to achieve sub-ms mixing dead time (~ 10 μs) and low sample consumption rate [47-51]. The principle of hydrodynamic focusing is that mixing is via diffusion and achieved by reducing the dimension of mixing region. Its applications in the study of kinetics of biomolecules arouse a lot of interests, especially in the research of protein folding. However, the velocity of flow (or travelling velocity of sample particles) plays an important role in time resolution of this continuous-flow mixing system. The nature of the parabolic flow velocity profile in micro-channels fails the sub-ms mixing dead time under the conventional wide-field imaging system due to the long depth of field. On the other hand, the lack of precise measurements on the velocity in micro-fluidics imposes more uncertainties on the time resolution. Confocal microscopy combining with correlation analysis is one of the solutions to this problem.

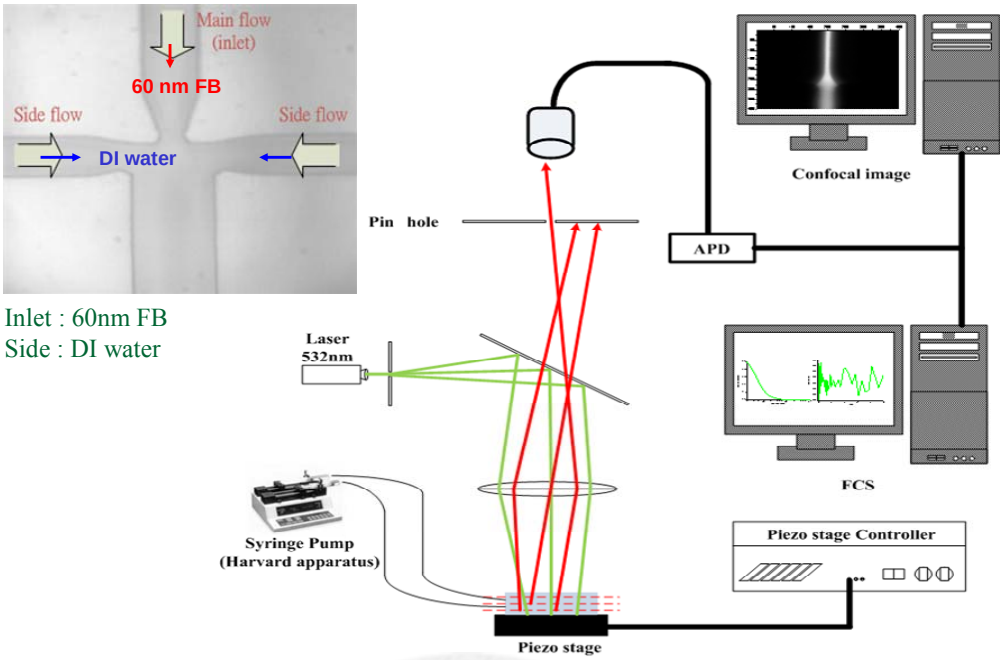

Figure 10. Schematic illustration of the optical system (confocal microscopy with FCS) [52]

This work is collaborated with Dr. Chien-Cheng Chang and Dr. Chin-Chou Chu in Institute of Applied Mechanics, National Taiwan University. They are responsible for simulations on momentum/mass transportation and fabrications of microfluidic mixing devices [52]. Figure 10 shows the schematic representation of the data acquisition system based on confocal microscopy and FCS. Our home-built confocal microscope can be switched to the wide-field mode to locate the cross regime of the mixer (left panel, Figure 10); the picture was taken by a charge coupling device (EMCCD 887-BUV, Andor Technology). Three inlet flows are driven by syringe pumps, and the flow rates are manually adjusted. The whole device is mounted onto the peizo-stage, and stage-scanning mode is used for confocal imagining. Fluorescence emission was detected by a photon counting module (APD, avalanche photo-diode, SPCM-AQR- 15-FC, PerkinElmar); the output TTL signals from APD were split into two channels and sent to the data acquisition card and the correlator (ALV-5000, ALV GmbH, Germany) respectively.

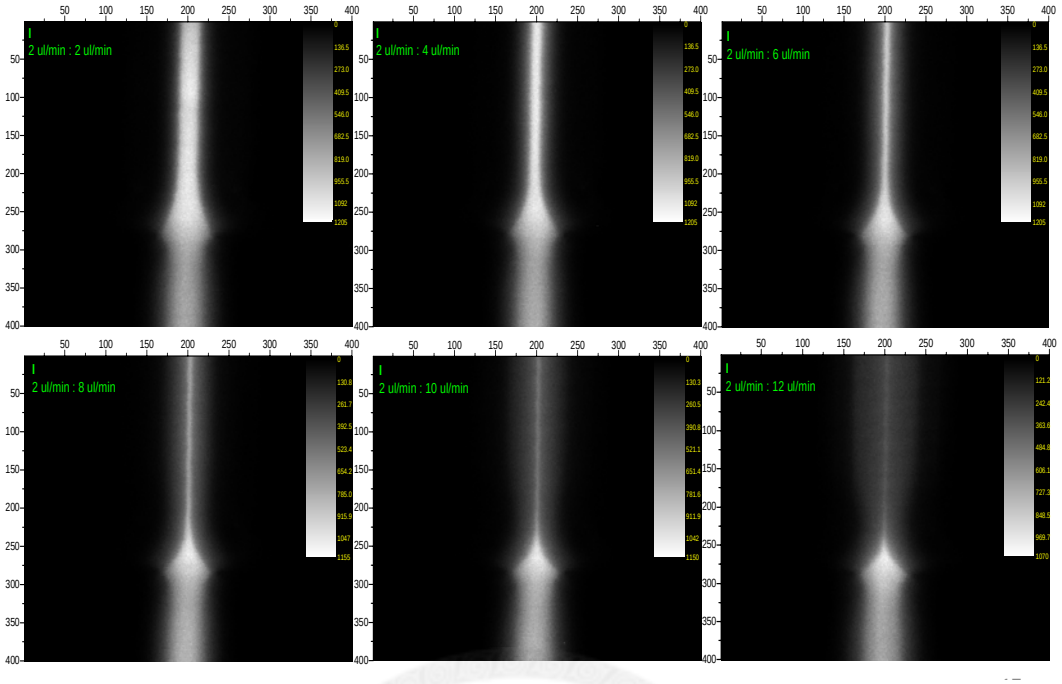

Figure 11. Demonstration of hydrodynamics focusing by 60 nm fluorescence microspheres [52]. The central flow carrying microspheres is squeezed by two side flows. The focusing width is decreasing with rising side flow rate.

Fluorescence microspheres (~ 60 nm in diameter) were injected into the microfluidic mixing device from the central inlet to demonstrate hydrodynamic focusing. Two side channels were loaded with DI water. Figure 11 is a series of confocal images with increasing flow rates of side channels. The higher the flow rates of side channels, the tighter the focused central flow which carried fluorescence microspheres. The focusing width was related to the derived mixing dead time; the relation between focusing width and side flow rate is plot in Figure 12.

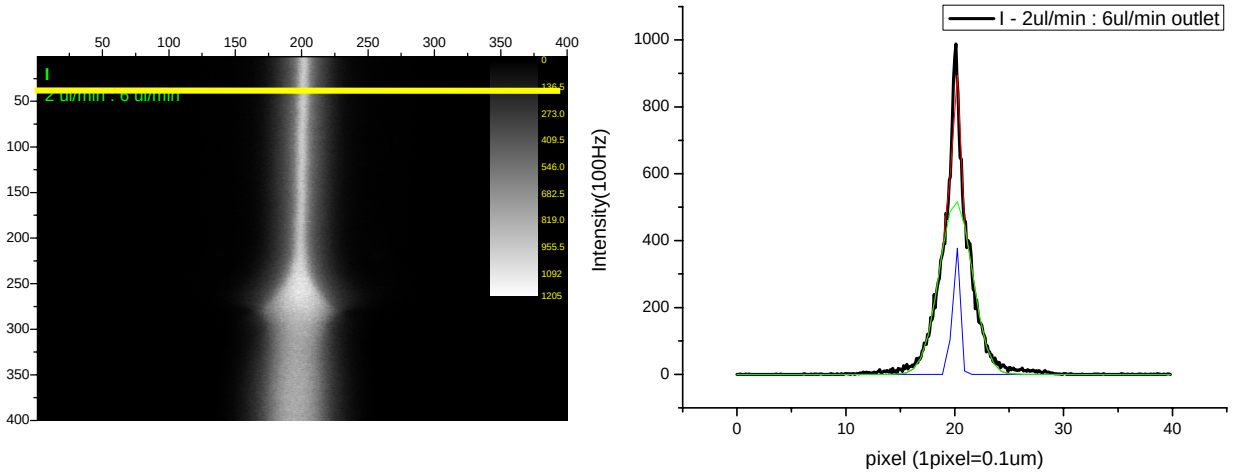

Main : Side (ul/min)	W_F (um)
2 : 2	2.3
2 : 4	2.2
2 : 6	0.60
2 : 7	0.64
2 : 8	0.60
2 :10	0.59
2 :12	0.65

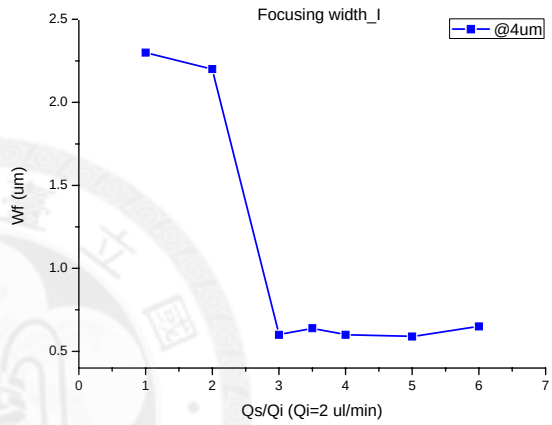

Figure 12. Determination of the focusing widths of the central flow at various flow rate ratios (F_M : F_S) [52].

However, the tightest focusing width did not promise the best time resolution since the particle travelling velocity in the squeezed central flow might decrease as the side flow rate goes beyond a certain value (6μl/min in our case) [53], Figure 13. The flow velocity (travelling velocity of the fluorescence microspheres) decreased with the increasing side channel flow rate, Figure 13 B.

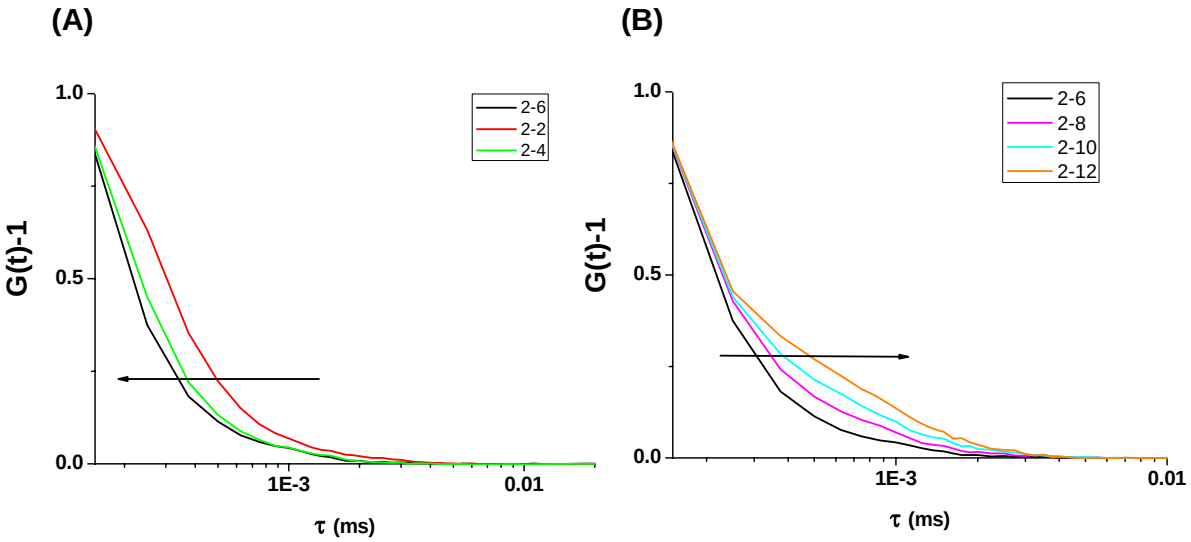

Figure 13. Normalized fluorescence autocorrelation function, $G^{(2)}(\tau)$-1, of squeezed central flow carrying with fluorescence microspheres. (A) The particle velocity of the central flow increases with the flow rate of side channel. (Arrow direction); (B) When flow rate of side channel goes beyond 6 μl/min, the particle velocity decreases [52].

The flow velocity (Figure 14) was obtained by fitting the cures with the equation concerning velocity and correlation analysis, Equation (29), and the value was 0.25 m/sec under the condition 2 μl/min : 6μl/min (main : side). The corresponding time resolution of this mixing device was ~ 4μs (the size of the optical diffraction spot is ~ 0.3 μm x 1 μm).

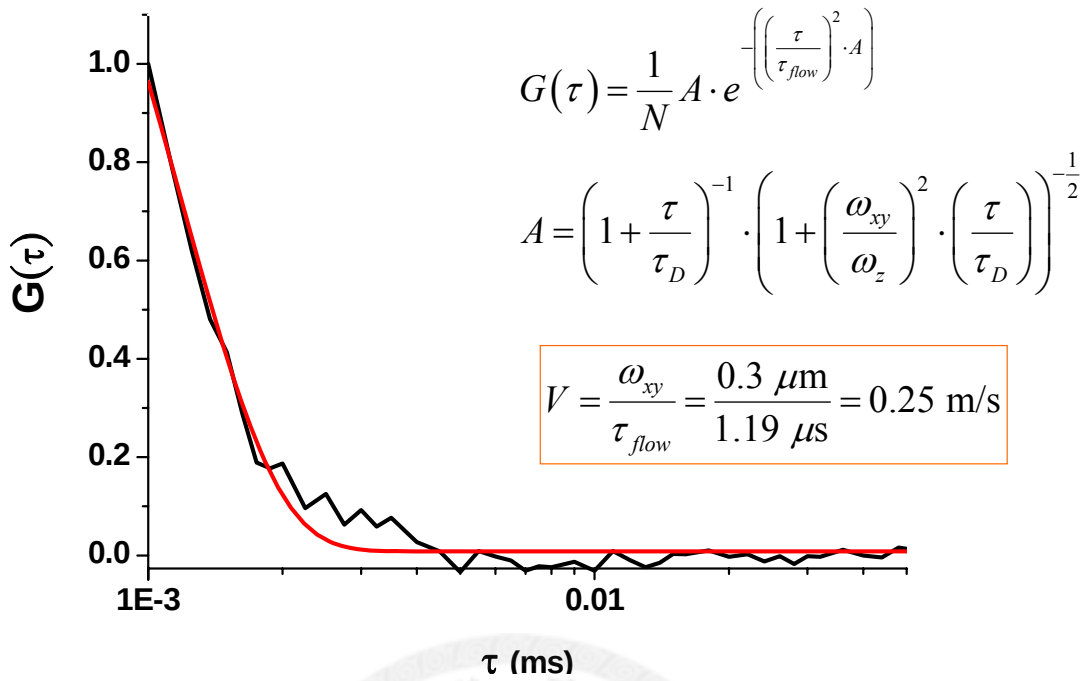

Figure 14. The velocity of the focused central flow obtained by fitting into the autocorrelation equation. The derived flow velocity is 0.25 m/sec.

3.3: Development of Real-Time Data Acquisition

A real-time correlation algorithm which is based on the inter-photon time taken by the data-acquisition card (National Instrument, PCI-6602) was established [54]. The algorithms were coded in ANSI-C language by Dr. J.D. White, and compiled in the form of dynamic link library (DLL). The user interface is programmed in LabView, which can call the DLLs. The flow chart of data acquisition is shown is Figure 15. A TTL pulse generated by the avalanche photo diode (APD) is used to gate the internal clock of PCI-6602 board. Four loops are involved in the data acquisition and processing. One is transferring the number of clock (τ) to the computer memory, and the other three are responsible for inter-photon arrival time histogram (hst), autocorrelation function (acf), and intensity time trajectory (tt) respectively.

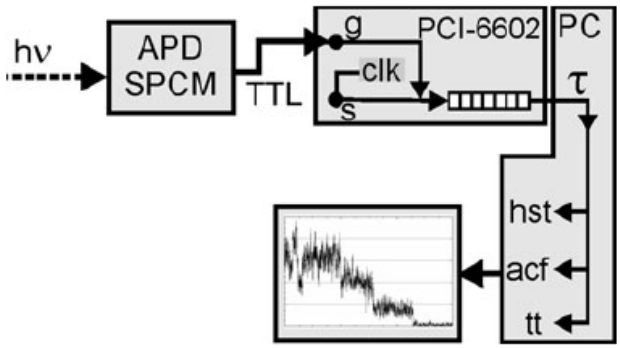

Figure 15. Flow chart of real-time data acquisition, processing and display system controlled by LabView [54].

All the data acquisition and calculation was done in the host computer which was connected to a guest computer via ethernet cable to display the results. Experiments of the diffusion of Rhodamine 6G ($D = 0.28\ \mu m^2 ms^{-1}$) was performed to examine the validation of the algorithm. Figure 16 is the comparison between the autocorrelation taken by the commercial correlator (ALV-5000, ALV GmbH, Germany) and our calculation algorithm. The curves were overlapped well and the information regarding the excitation focal volume were derived by fitting to the 3D diffusion model.

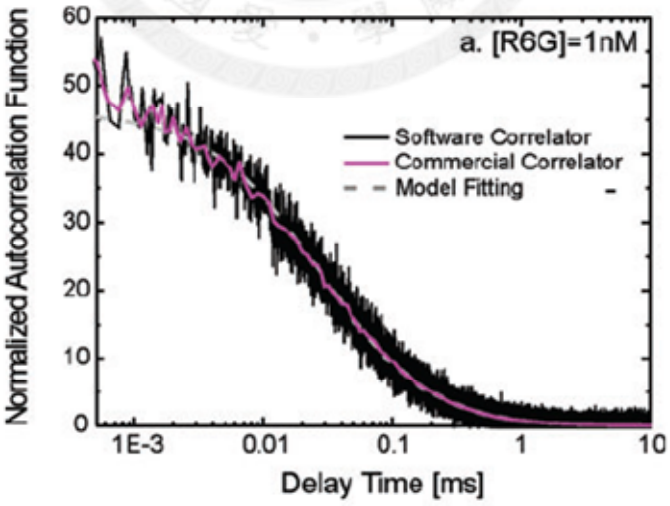

Figure 16. The calculated autocorrelation function of the fluorescence time trace of ~ 1 nM R6G [54].

The direct approach to calculate the autocorrelation function (acf) is making use of the number of incoming TTL pulse in a given time interval. Some hardware based correlator which employed either fast electronics or varying time resolution (multi-τ algorithm) to reduce calculation is applied to improve computation efficiency. The inter-photon times from the data stream are used to update the autocorrelation function (acf) in real time. Only two arrays are used, one to hold the autocorrelation function (acf), and one (delay) that serves as the indicators of the elements of "acf" needed to be updated after the arrival of the new photon.

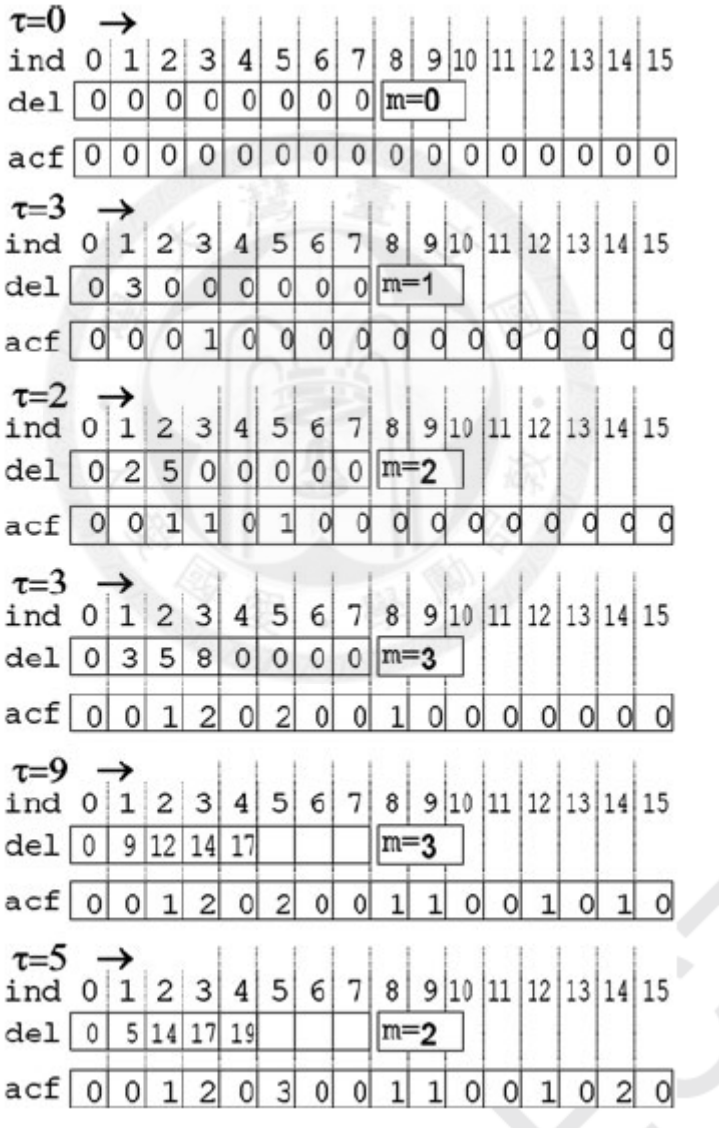

Figure 17. Sample calculation of the raw autocorrelation function of six photons [54].

To illustrate the principle of the algorithm, a sample calculation of the autocorrelation function of six incoming photons was demonstrated, Figure 17. Assume that a series of arriving photons have corresponding inter-photon time, $\tau = \{0, 3, 2, 3, 9, 5\}$, and mtau = 15 clock cycles. The inter-photon time were registered as 3 in the array "del" when the second photon arrived, and added "1" in the corresponding clock cycle in the second array. When the third photon came, the number registered in "del" was shifted leftward and was added to the new inter-photon time. At the same time, the new inter-photon was recorded in position "1". According to the values of two new derived delay times, we added "1" to the corresponding clock cycle respectively. The autocorrelation function was thus constructed with the arriving photons.

3.4: Applications of TCSPC

3.4.1:The Number of Chromophores of DO-PPV Aggregates

A start-stop experiment based on Hanbury Brown – Twiss photon correlation analysis was performed to observe the number of emitters of each single DO-PPV aggregate [27]. The single aggregate was excited by 532 nm pulse laser, 50 MHz of repetition rate, and the excitation power was ~ 0.3 μW. The single chain of DO-PPV served as a comparison for DO-PPV aggregate. To excite single-chained DO-PPV, 460 nm pulse laser with 76 MHz of repetition rate was in use (~ 0.5 μW). Fluorescence emissions were collected by an oil immersion objective (X100/N.A. 1.3 oil), divided by a 50/50 beam splitter, and detected by two single photon counting modules (avalanche photo diodes) respectively. The signal from the first APD was regarded as the "start" while that from the other was the "stop". The arrival time difference between each pair of "start" and "stop" signal was recorded by a time correlated single photon counting (TCSPC) board (Becker & Hickle GmbH, SPC-600). The interphoton time histogram of arriving photon pairs was constructed to characterize the average number of emitter of a single molecule. Figure 18 includes the interphoton time histograms of single chain of DO-PPV and DO-PPV aggregate, which shows the "anti-bunching" phenomenon. Since the repetition rate of 460 nm pulse laser is higher than that of 532 nm, there are more peaks observed for DO-PPV single chain in the same time window (150 ns). There were less chromophores existing in single-chained

DO-PPV in average, which resulted into less fluorescence emission and deeper anti-bunching dip.

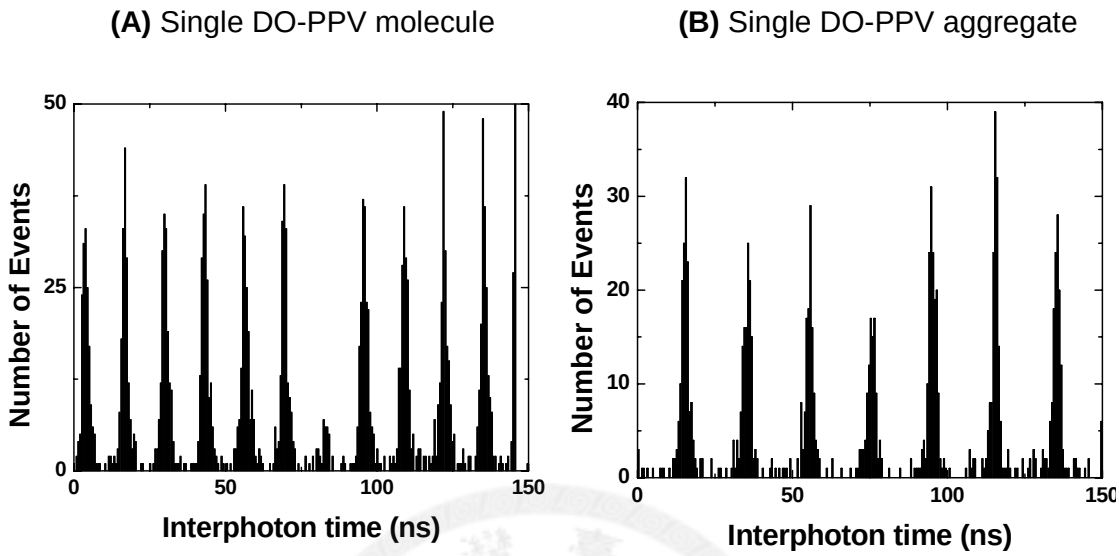

Figure 18. Interphoton time histogram of (A) Single DO-PPV molecule and (B) Single DO-PPV aggregate

$$g^{(2)}(\tau = 0) = \frac{A_{central}}{< A_{side} >} = 1 - \frac{1}{N} \tag{36}$$

$$N_{corr} = N \cdot (1 - \frac{I_{BG}}{I_s - I_{BG}})^{-2} \tag{37}$$

In addition, the effect brought by background intensities should be taken into account as well. The "real" number of chromophores were determined according to Equation (37), where N_{corr} is the calibrated number of emitters, N is the measured, and I_S and I_{BG} are the intensities of signal and background respectively. Here, I_{BG} was determined by a blank cover glass as a control in advance.

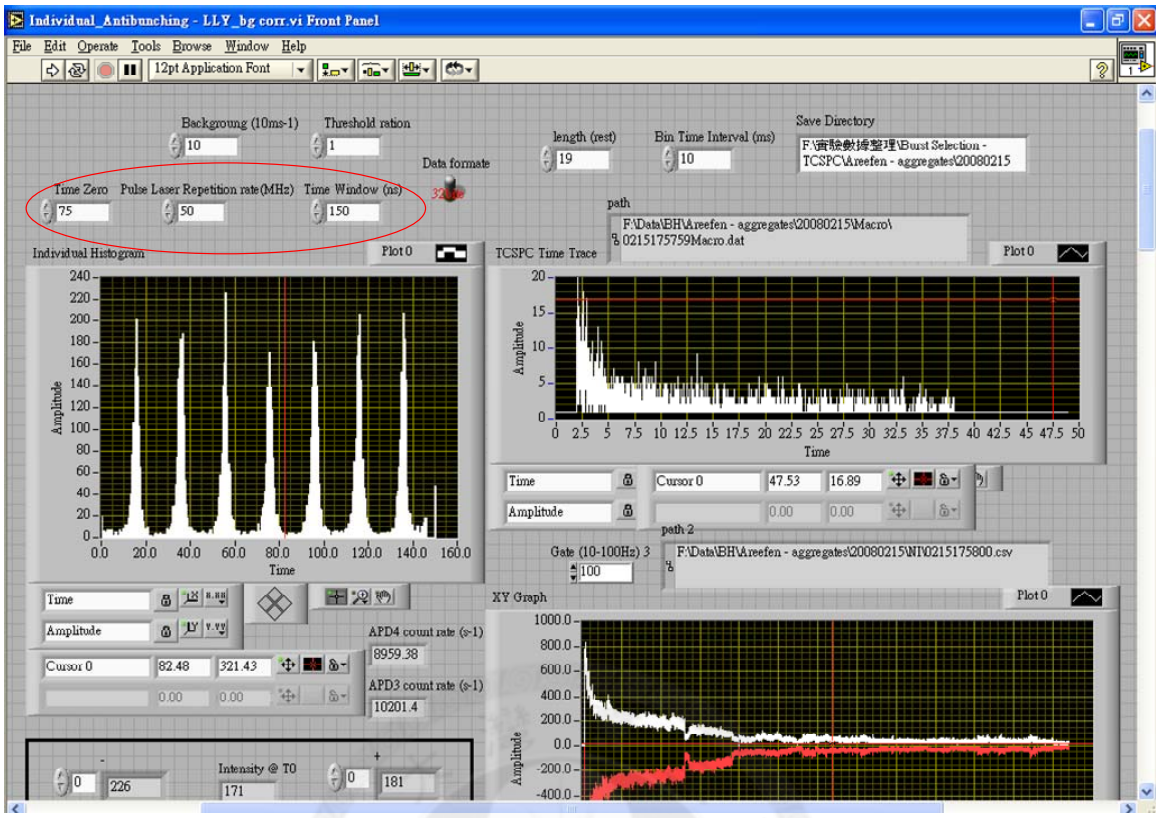

Figure 19. Upper panel of the analysis software programmed in Labview to calculate the number of emitters in a single molecule under investigation. Both the intensity trajectories taken by NI DAQ card and TCSPC counting board are shown. The input parameters include the repetition rate of pulse laser, duration of the time window (ns), and pre-determined time "zero" (It is usually adjusted in the middle of the time window).

To construct the distribution of number of emitters, a great number of molecules were detected and analyzed. One of my main works was to develop the program to do batch-analysis for all detected molecules. Figure 19 and Figure 20 are the snapshots of the panel of the analyzing program. The analyzing program read the fluorescence time trajectory according to the anti-bunching curves loaded, and selected and calculated the two peak value (area) next to the time zero. The input parameters included the repetition rate of the pulse laser, duration of the time window (ns) and the position of time zero with respect to original "0", Figure 19. The calculated number of emitters which had the background calibrated was also shown in the panel, Figure 20. The arriving time difference of two channels was assigned as the time zero, and it could be adjusted by insertion of a delay line. Generally, it is sifted to the time half the time window.

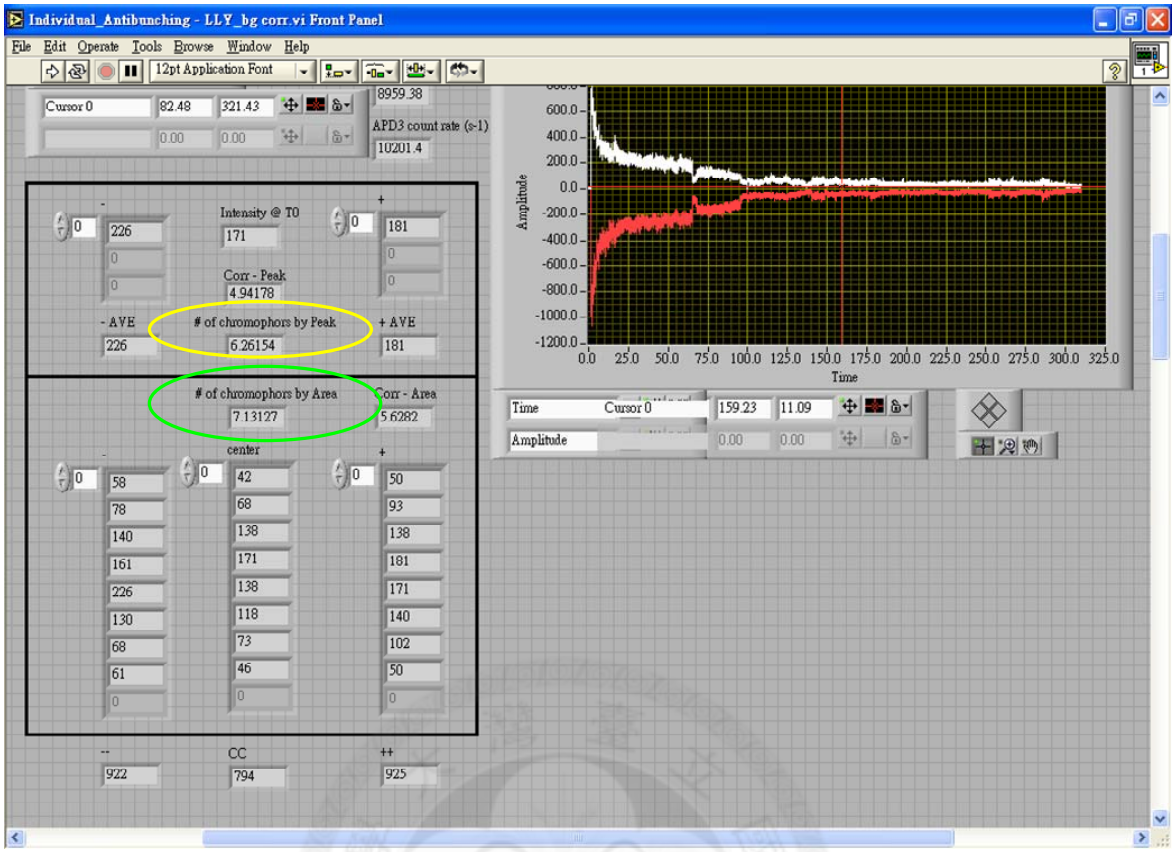

Figure 20. Lower panel of the analysis software programmed in Labview to calculate the number of emitters in a single molecule under investigation. The calculated number of emitters is shown.

The program was programmed to process all the traces and anti-bunching curves automatically, and the number of emitters of each molecule was recorded to construct the final distribution. (The path of the save directory should be provided.) Two statistics of different samples are shown in Figure 21.

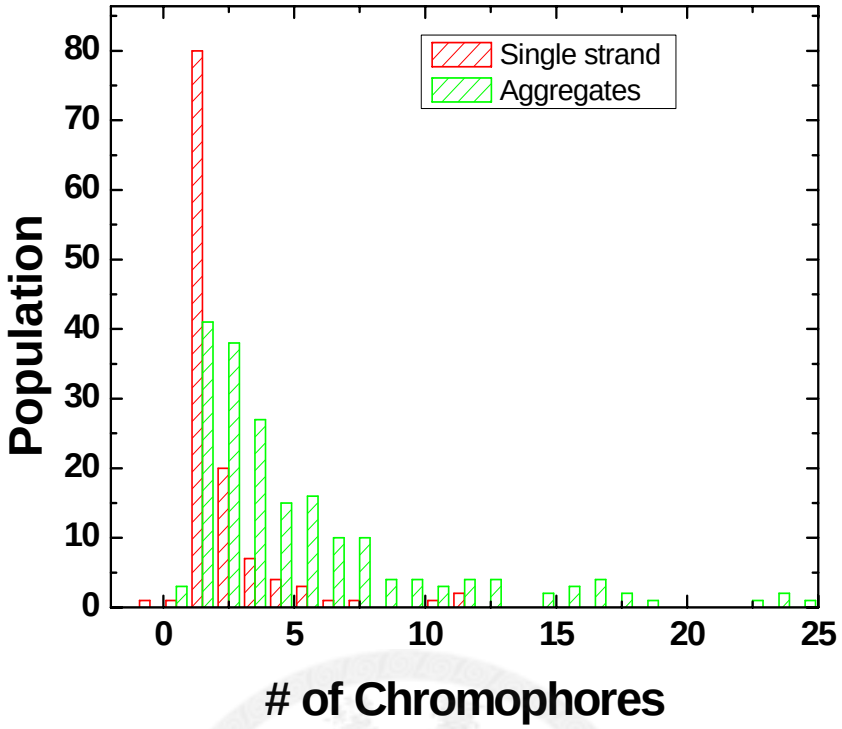

Figure 21. Statistics of the number of emitters of single-stranded DO-PPV and DO-PPV aggregates.

Figure 21 shows the distribution of number of emitters for single-stranded DO-PPV (red) and aggregate of DO-PPV (green). It was obvious that most of the single-stranded molecules were populated at the number of chromophores equalling to "1" while aggregates of DO-PPV had broader distribution and more number of emitters in average.

3.4.2: Fluorescence Intensity Burst Analysis

In addition to measurements on the number of chromophores of an immobilized single molecule, TCSPC (time correlated single photon counting) can also have wide applications on molecules in solution, especially for the diluted samples.

The structural properties of amyloid fibrils, which might result into the brain-related diseases, such as Alzhermer's disease, have been studied extensively by a hydrophobic organic dye, ThT (thioflavin T) [55, 56]. Relative rotational freedoms of the two rings on ThT could lead to the low fluorescence quantum yield. Yet, the hydrophobic amino acid side chains of amyloid fibrils restrict the rotation of the two rings such that fluorescence quantum yield of ThT increases due to its insertion into the fibrils.

Changes of fluorescence quantum yield can be characterized by either fluorescence emission intensity or fluorescence decay lifetime. Fluorescence decay lifetime is a direct way with less confusion from background signals, and hence adopted as the experimental tool usually.

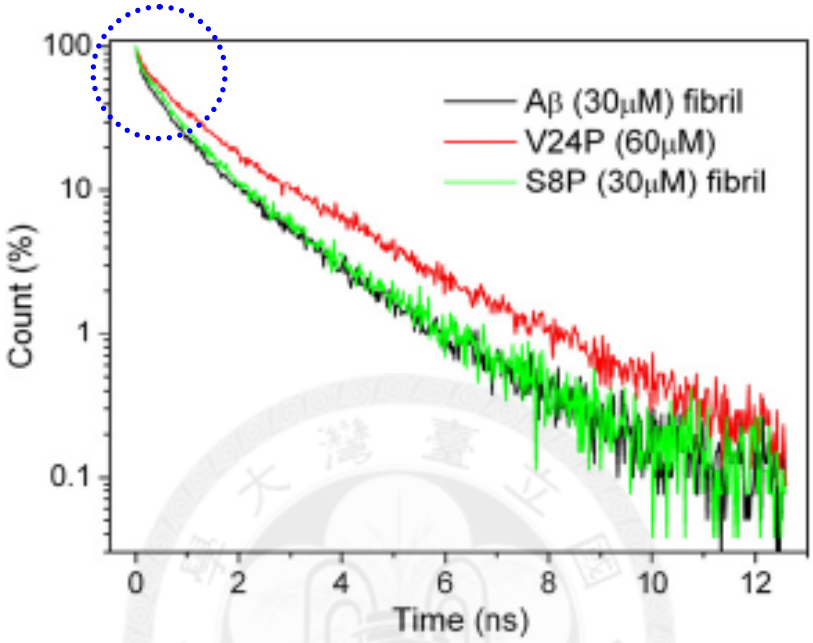

Figure 22. Fluorescence lifetime decay of ThT bound to three different fibrils [57]. The circles in blue dashed line points out the burst phase which might be resulted from free ThT.

Free ThT molecules in solution though less fluorescent might still contribute to the burst-phase in the lifetime decay measurement [57], Figure 22, and could be confused as the heterogeneous fibril structures. To solve this problem, a post-processing software programmed in Labview was developed based on TCSPC, Figure 24. In the data acquisition of TCSPC, two characteristic time scales are recorded by the single photon counting board. One is termed as “micro-time”, which is the time difference between the first detected photons and trigger signal of the pulse laser. The other is called “macro-time”, which is referring to the arrival time of every detected event (photon) with respect to the starting time “zero” of the counting board. A representation of the idea of time correlated single photon counting is illustrated in Figure 23.

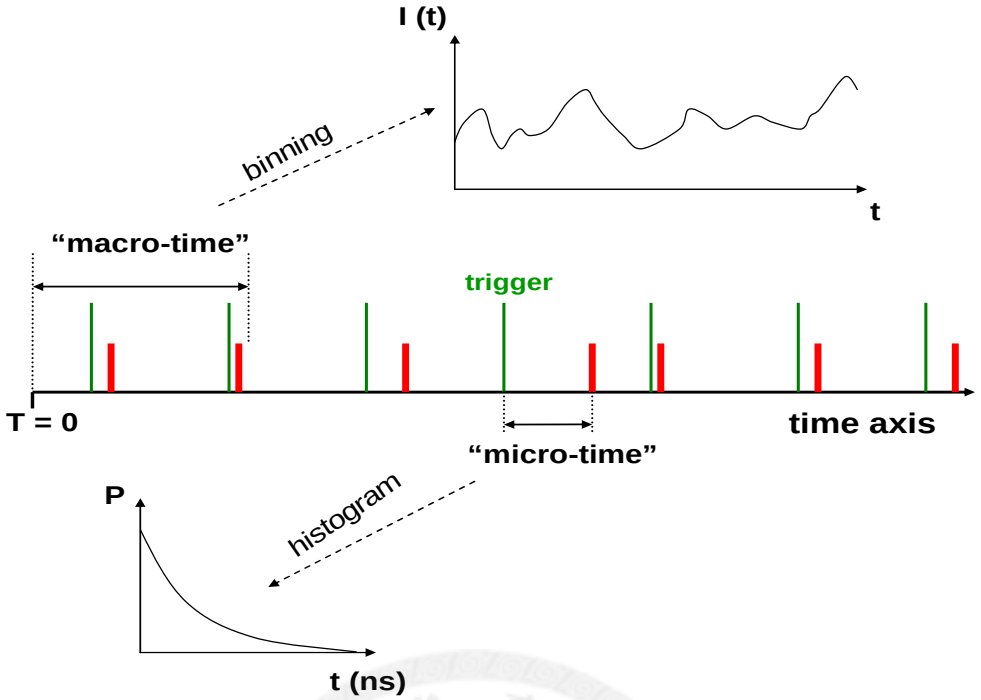

Figure 23. Cartoon representation of time-correlated single photon counting (TCSPC)

By summing up the photon numbers at each time bin (manually defined), the intensity time trajectory was retrieved as the left panel, Figure 24. As the chopped ThT tagged fibril swam through the excitation spot, a corresponding fluorescence burst was recorded accordingly. An intensity threshold was imposed to distinguish signals from the background noises, and the “macro-times” of those selected signals were counted in for the lifetime decay histogram, Figure 25. It was obvious that the burst phase in the early beginning of lifetime decay disappears. Fluorescence burst analysis could not only be applied to the samples which might have meaningless and confusing non-radiative decay channels, but also practical to take lifetime measurements on diluted samples.

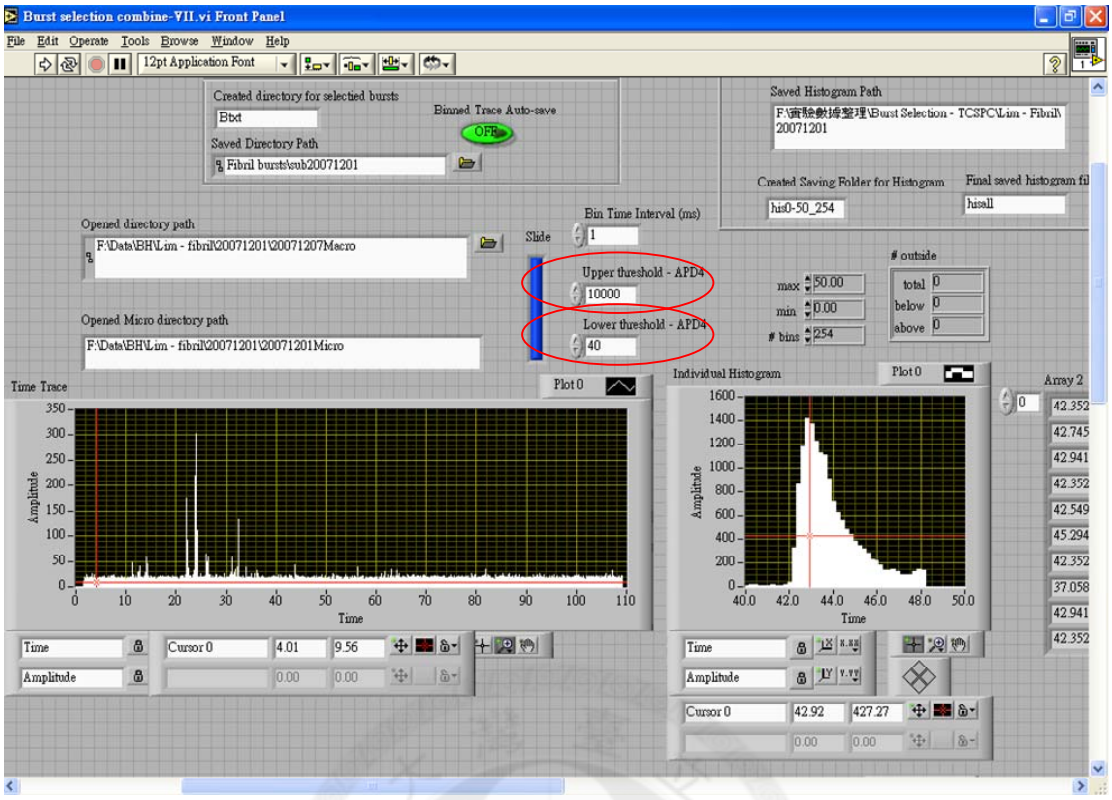

Figure 24. Fluorescence burst analysis software programmed in Labview.

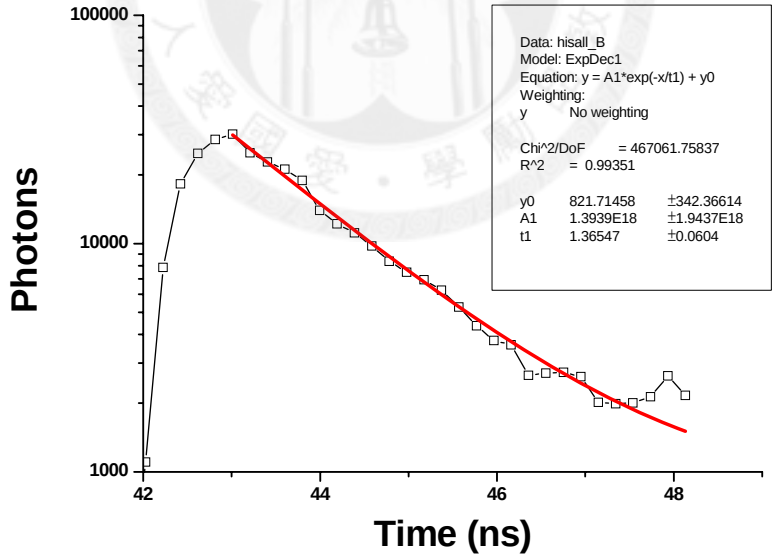

Figure 25. Lifetime decay histogram of chopped amyloid fibrils constructed by the software of fluorescence burst analysis.

3.4.3: Fluorescence Intensity Burst Analysis on FRET

The idea of fluorescence burst analysis can be further modified to fit in with the applications of FRET [58, 59]. When protein molecules labelled with the FRET dye pair are passing through the excitation focal volume, the corresponding fluorescence intensity bursts at donor and acceptor channels are observed. Though conformational dynamics is missing in free solution experiment, the distribution regarding conformations etc. can still be obtained. Furthermore, with the help of TCSPC or TTTR (Time-Tag Time Related single photon counting), the distribution can be categorized according to the FRET efficiencies.

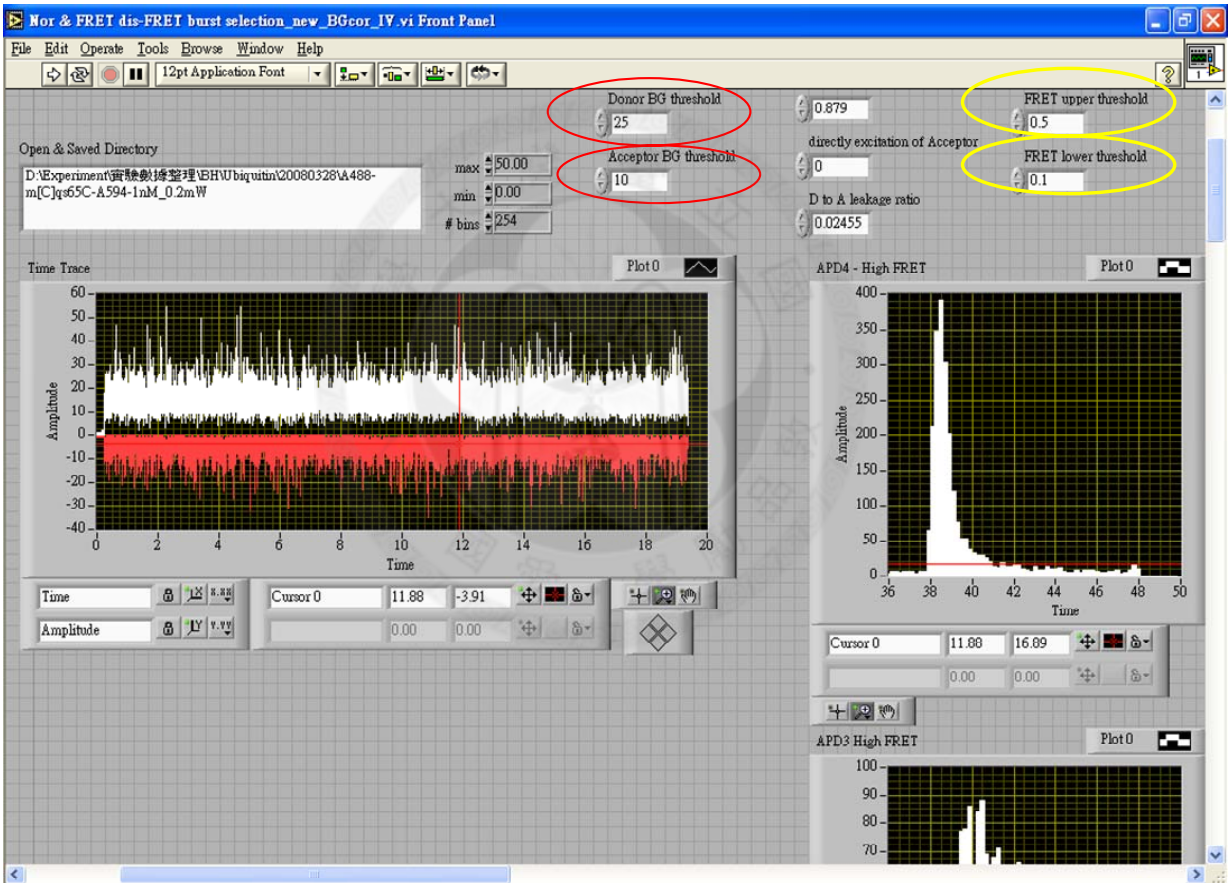

Figure 26. (Left-hand-sided panel) The software of fluorescence intensity burst analysis for FRET programmed in Labview. Input parameters include: (I) intensity thresholds for donor and acceptor channels to distinguish fluorescence emission from background noises (Red circles); (II) thresholds for FRET efficiency (upper and lower) to divide populations into three (Yellow circles).

Firstly, the fluorescence signals of donor and acceptor channels are selected out of background noises according to the algorithm that either donor or acceptor higher than its own intensity threshold, both of donor and acceptor are counted in. Then, each pair of donor-acceptor fluorescence burst is transferred into FRET efficiency, and further divided into three categories: low FRET (FRET < 10 %), middle FRET (10 % < FRET < 50 %), and high FRET (FRET > 50 %), Figure 26.

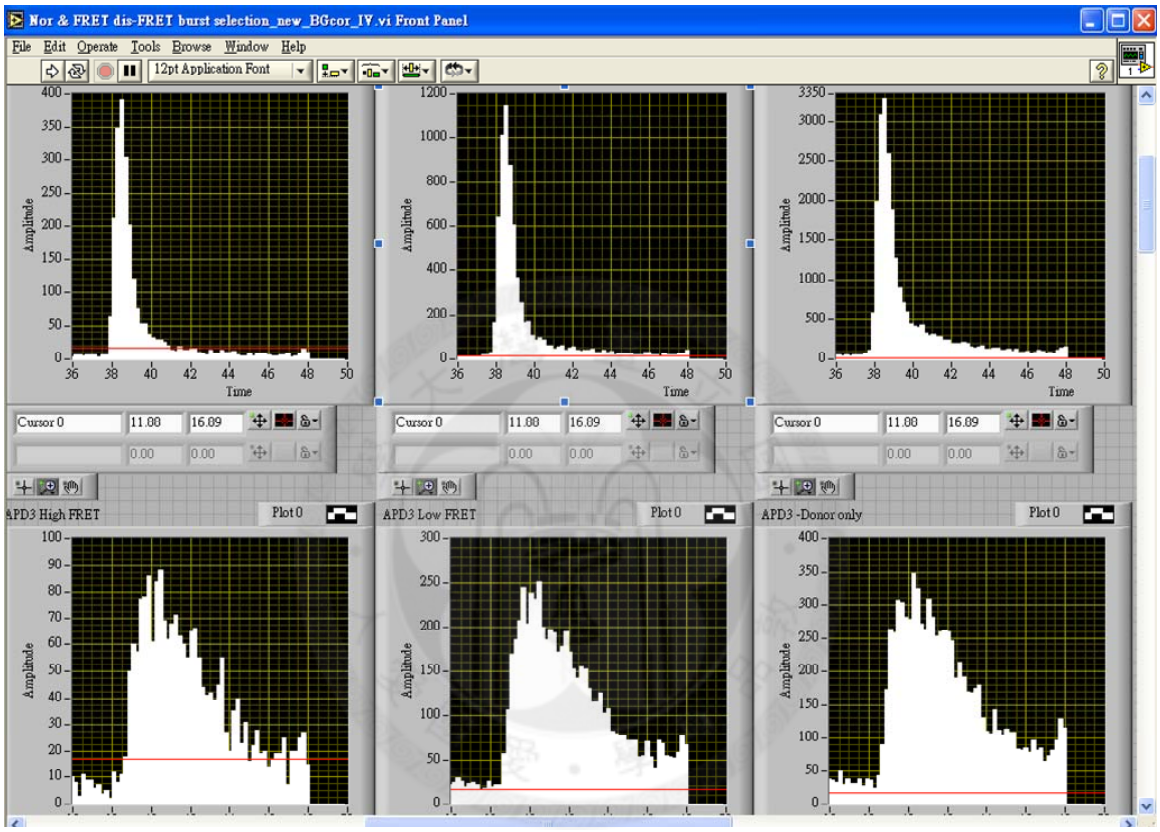

Figure 27. (Right-hand-sided panel) The software of fluorescence intensity burst analysis for FRET programmed in Labview. Donor and acceptor lifetimes for different categories (by FRET efficiency).

"Micro-times" of donor and acceptor corresponding to the selected signals are recorded and put into different lifetime decay histograms according to their FRET efficiencies, Figure 27. The comparison of donor and acceptor lifetime decay cures among three FRET types is shown in Figure 28, and so does the FRET population distributions.

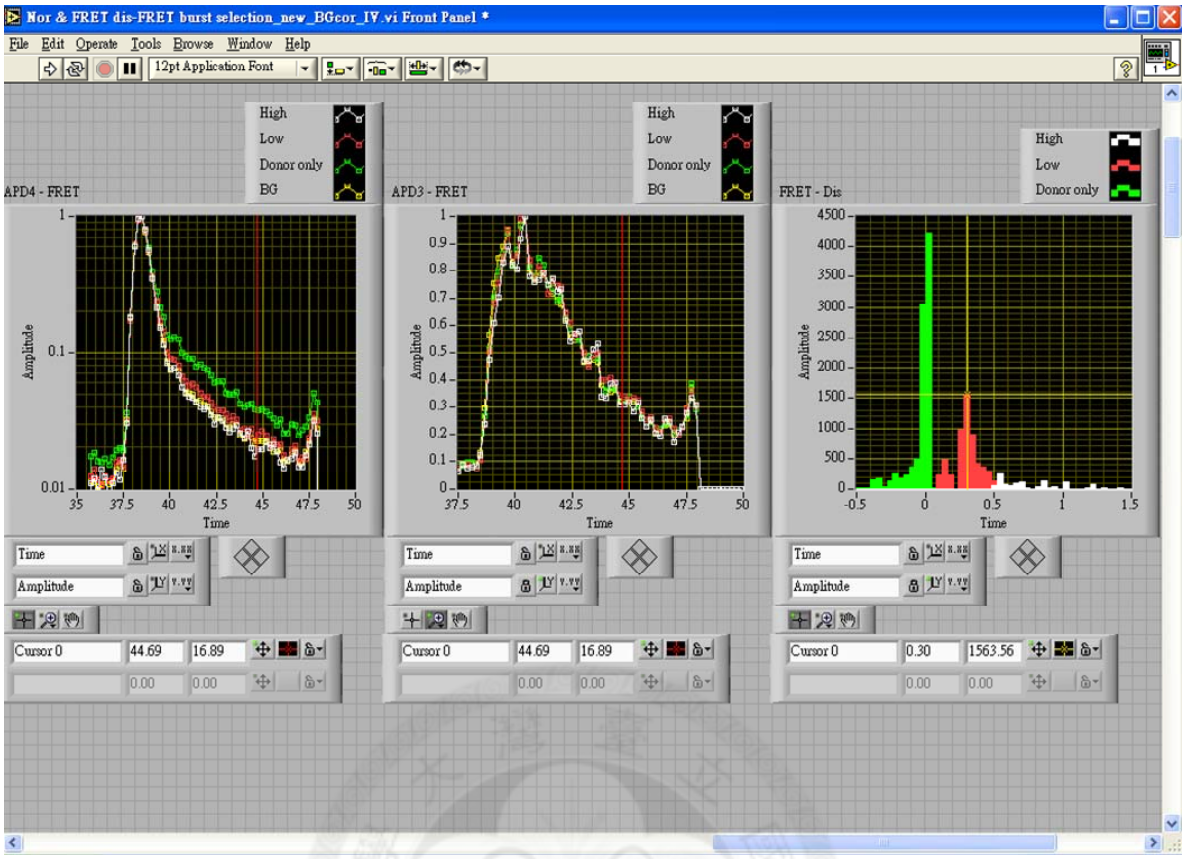

Figure 28. Comparison of donor and acceptor lifetime among three different types of FRET. The corresponding FRET populations are shown at the panel on the right.

The population hump in the early lifetime decay was resulted from the high background fluorescence since 460 nm pulse laser was used to excite Alexa Flour 488. Though burst analysis could help eliminate contributions from background shot noises, the interference from the DC background fluorescence could not be removed thoroughly. On the other hand, we also try to obtain information from acceptor lifetime, especially for the low FRET population. The acceptor lifetime is obtained by accumulating time durations between the first detected photon and the trigger of the pulse laser in the acceptor channel. A gradual building-up transition due to FRET was expected in acceptor lifetime, especially for low FRET cases, Figure 29. The presence of acceptor provides the electron in the excited state with another relaxation channel to release its energy. Assume that both the donor and acceptor have the lifetime as ~ 3 ns. According to Equation (3), the characteristic time of FRET ($1/\kappa_{FRET}$) varied from 2.5 ns to 0.33 ns when FRET efficiency changed from 10 % to 90 %.

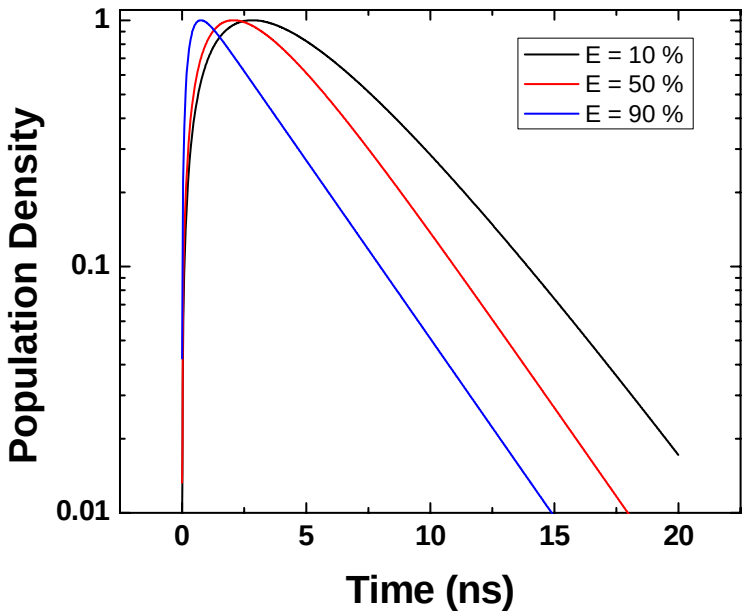

Figure 29. Comparison of acceptor lifetimes at different energy transfer efficiencies [60].

Two factors are competing at the very beginning of electron relaxation in acceptor cannel. One is radiative (and non-radiative) decay; the other is the FRET. The net effect is that the peak of the decay curve is shifted with the following decay unchanged. However, no distinguished displacement was observed in the experiment. That might be because the system response which was assumed to be a δ-function in the simulation could obscure the lifetime decay at the very beginning.

CHAPTER 4

INVESTIGATIONS ON UBIQUITIN BY spFRET

Ubiquitin's highly structured native state and stability makes itself a mainstay of the studies on protein folding [61] and engineering. Protein folding is a long-held problem of great importance [62]. However, available information regarding the structural evolution upon folding is still insufficient. We would like to approach this issue from the perspective of single-molecule detection incorporating spFRET. The first step is to study the behaviour of the specifically dye-labeled ubiquitin mutant, m[C]q/S65C, in equilibrium. Investigations on surface-immobilized ubiquitin molecules and in free solution were also performed. According to our observations, conformational heterogeneity of dye-labeled ubiquitin was suggested.

Introduction to the strategy of dye-labeling is illustrated in section 4.2. In section 4.3, characterization of structures on ubiquitin with/without dye-labeling is described. Experimental details are listed in section 4.4; results and discussion are pursued in section 4.5.

4.1: Introduction to Ubiquitin

Ubiquitin is a small globular protein with 76 amino acids, which is of great importance not only because of its being ubiquitous in cellular environment but also its favorable properties – high stability in a wide range of pH value and temperature [63]. The effect of salts and surface charges on ubiquitin's stability was firstly explored [64, 65], and detailed analyses of the hydrophobic core via protein engineering followed up [66-68]. The range of stabilities ($\Delta\Delta G_{D\text{-}N}$s, the unfolding free energy difference between wild type and mutants) is from -1.7 kcalmol^{-1} to +4.4 kcalmol^{-1} [69], and the hydrophobic interactions play the most important role in the stability. The removal of surface charge-charge interactions still leaves the protein folded [70] whereas mutations of buried hydrophobic core residues generally destabilize the native state with the exception of substitution of Val26 by Ala [66]. How to correlate the stability to the corresponding structure and then to the functions of proteins is one the vital issues in protein science. Especially, these favourable properties might have some connections to its unique functions [71].

4.1.1: History of Ubiquitin

Ubiquitin was first isolated from the thymus by Gideon Goldstein et al in 1975, and named for its being ubiquitous and conserving in all tissues and eukaryotic organisms. On the other hand, Avram Hershko [72] who was studying regulation of tyrosine aminotransferase found that the degradation of the enzyme was arrested by inhibitors of cellular energy production. It was the first finding on the existence of an energy dependent proteolytic system. In the following ten yeas, Hershko was devoted into the study on this energy-dependent system responsible for protein degradation, which gradually aroused general interests on the role of ubiquitin especially in protein degradation. In addition to protein degradation, ubiquitin is also involved in some other essential regulatory processes, such as modulation of transcription, translational and protein localization et al.

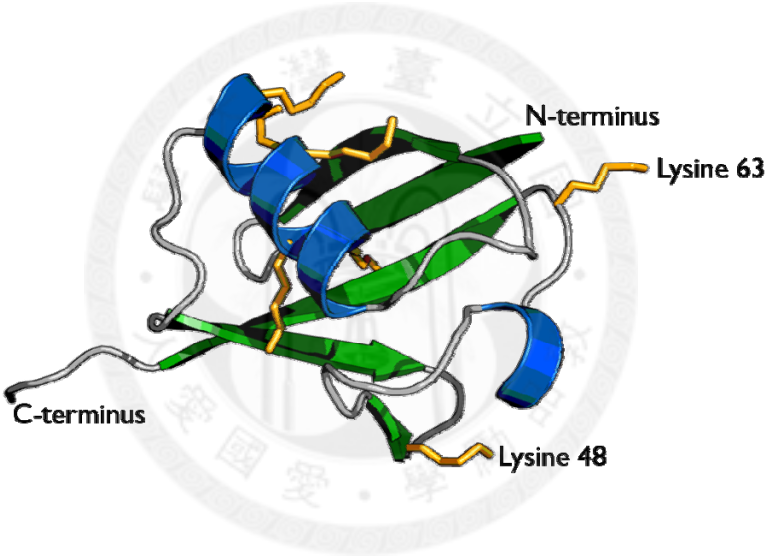

Figure 30. Secondary structure of Ubiquitin

4.1.2: Ubiquitylation

In the cell ubiquitin serves as a "label" to target a substrate protein. Ubiquitn appends onto the target protein via the formation of isopeptide bond between C-terminal Gly of ubiquitin and Lys of the target protein. Two main steps are involved in protein degradation by ubiquitin system: (I) Ubiquitylation – covalently attachment of ubiquitin molecules to target proteins; (II) Degrading by the 26S proteasome [72, 73]. Ubiquitylation is via the isopeptide bonds between the internal Lys and C-terminal Gly of a ubiquitin molecule, and there are seven Lys residues. Ubiquitylations involving different Lys residues target to

various binding sites and lead to diverse functions. Figure 31 A is the ubiquitylation via Lys 48 and the illustration in panel B is via Lys 63. The conjugation with Lys-48 relates to protein degradation while that with Lys-63 participates in the activation of transcriptional regulators.

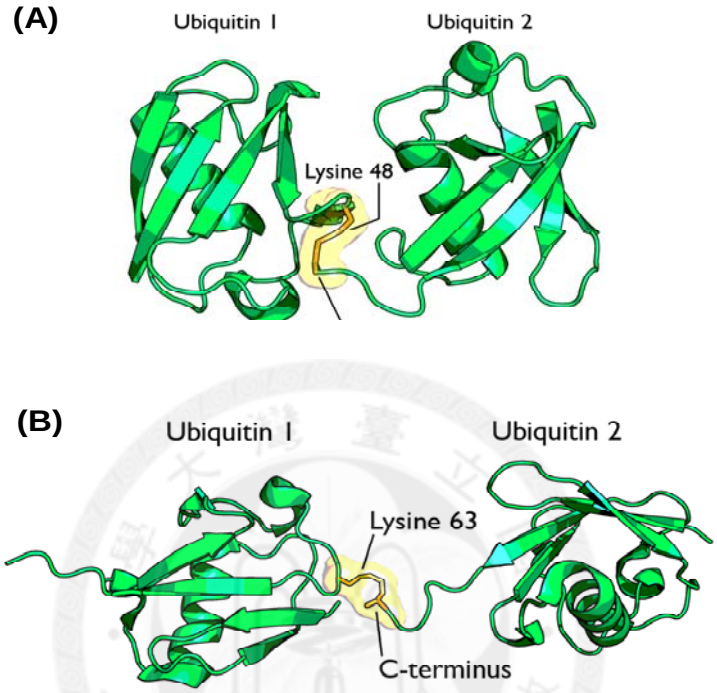

Figure 31. Two examples of ubiquitylation via different sites. (A) Lysine 48 (B) Lysine 63

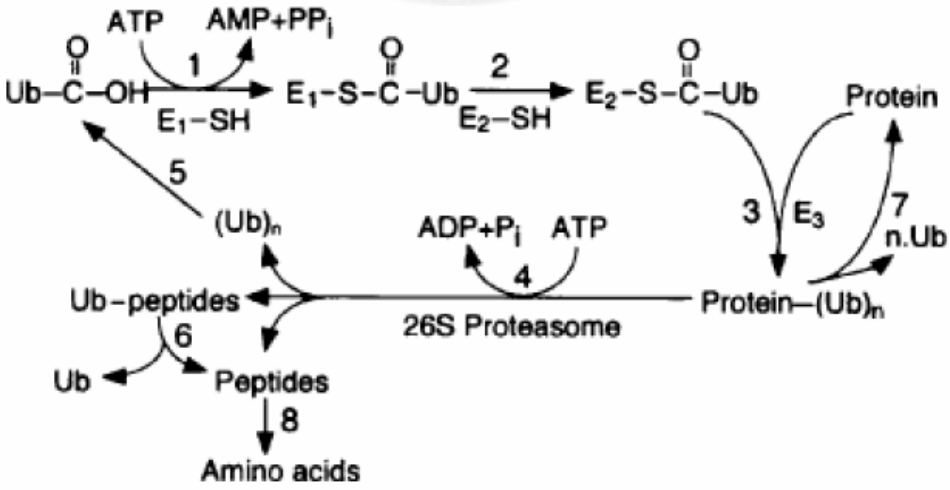

Figure 32. Ubiquitin proteolytic pathway [72]

Protein degradation is the most well known process about ubiquitin system [72-74]. Figure 32 is the ubiquitin proteolytic pathway, in which E2 is the activating enzyme, E2 is the conjugation enzyme, and E3 is the ligase. Ubiquitin binds to E1 at first, and is transferred to E2 in the following. With the help of E3, E2 is detached and ubiquitin binds to the target protein. After the poly-ubiquitin chain is formed, the degraded protein with ubiquitin tag is sent to 26S proteasome to be degraded. Ubiquitin molecules are released and can be re-used.

4.2 : Dye-Labeling on Ubiquitn

4.2.1: Design of labelling sites

Haas and coworkers [75] measured the reactivity of six Cys in adenylate kinase by determining the rate constants for the reaction of the six single-Cys mutants with 5,5'-dithiobis(2-nitrobenzoic acid), then chose one highly reactive cysteine and one less reactive cysteine as the labeling sites. Based on the measured reactivity, they showed that the reactivity of reaction sites could be predicted using a computer program[76]. Here, we chose the 76 amino acid protein, ubiquitin, which has no cysteine residues, as our target and used commercial software to predict the site-chain solvent accessibility of different sites after mutation to Cys. The calculation was executed by using Discovery Studio software (version 1.7, Accelrys, USA). The mutated protein was modeled based on the x-ray structure of ubiquitin (PDB code: 1ubq) and the resulting structure was simulated by using the Standard Dynamics Cascade protocol. For 20 energy-minimized structures, solvent accessibility was calculated. Solvent accessibility calculates the Solvent Accessible Surface (SAS) of protein atoms and residues. The Residue Solvent Accessibility is the sum of the surface of all atoms, including the backbone atoms, in the residue. The Side-Chain Solvent Accessibility is the accessibility for just the side chain atoms. The Percent Solvent Accessibility is the Residue Solvent Accessibility divided by the residue solvent accessibility of the fully exposed residue calculated using the extended gly-X-gly tripeptide, where X is the residue of interest.

We aimed to add one Cys in the N-terminal region and one in the C-terminal region. One ubiquitin mutant with a single Cys insertion between Met1 and Gln2, named m[C]q,

was predicted to have a higher solvent accessibility. Its side-chain solvent accessible surface was predicted as 56.1 ± 8.7 Å and the percentage of residue solvent accessibility as 46.5 ± 7.3 % based on twenty energy minimized structures. A Ser65→Cys mutant, named S65C, had a predicted side-chain solvent accessible surface of 28.0 ± 7.0 Å and a percentage of residue solvent accessibility of 21.0 ± 5.4 %.

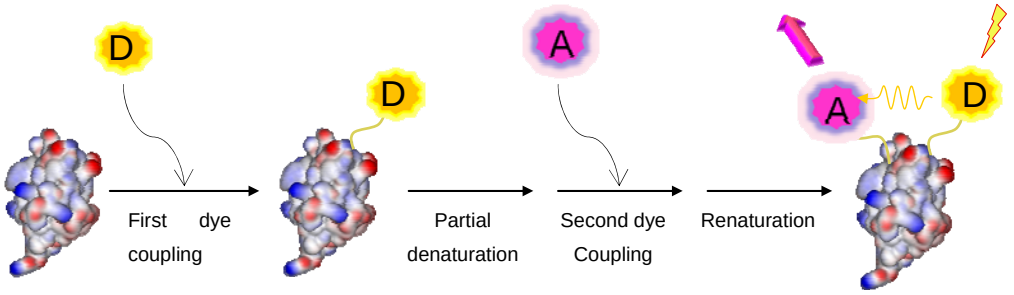

Figure 33. Schematic representation of double dye-labelling [77]

4.2.2: Design of solid-phase labeling strategy

Another important feature of our strategy is the use of magnetic beads, which can tolerate high concentrations of denaturants, such as 6 M GdnHCl and 8 M urea. The advantages of carrying out the reaction on a solid support include: (1) avoiding disulfide bond formation in the protein; (2) easy removal of free dye after reaction for reuse, thus saving on cost; and (3) avoiding protein aggregation under partially denaturing conditions. A 6-His tail was added to the end of ubiquitin for bead binding

An efficient double dye-labeling method was developed for FRET studies of ubiquitin. An ubiquitin mutant with two Cys mutations, one with high solvent accessibility and the other with low solvent accessibility, was constructed. The first dye reacts with the Cys with the high solvent accessibility and the second with the other Cys under partially denaturing conditions. binding. For the dye pair, we selected Alexa Fluor 488 and Alexa Fluor 594 as our donor and acceptor dyes, respectively. The scheme of solid-phase labeling strategy is shown in Figure 34.

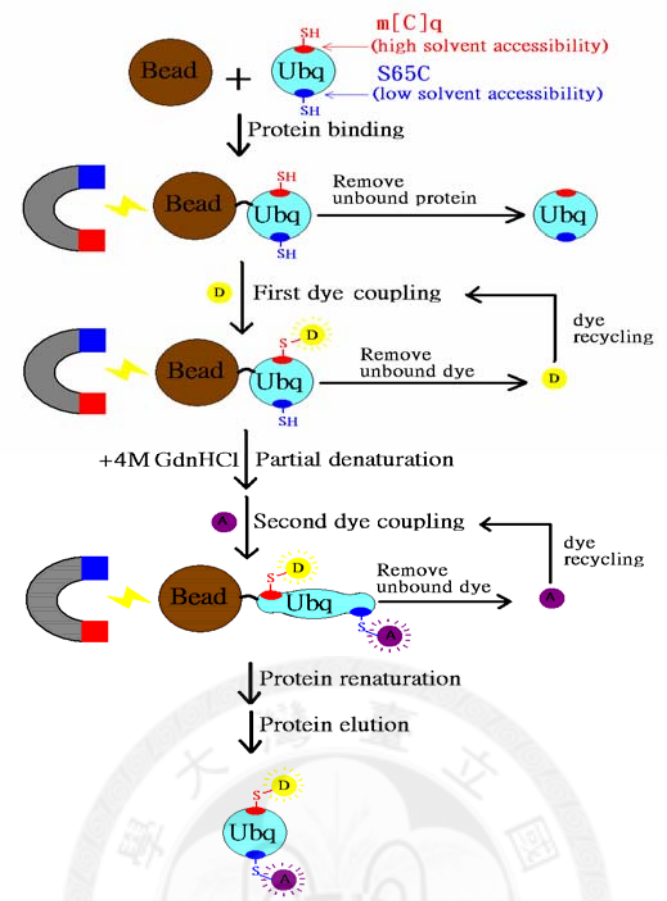

Figure 34. Solid-phase labeling strategy [77]

4.2.3: Coupling efficiency of the designed labeling sites

The mutant proteins m[C]q and S65C were expressed separately. As predicted, m[C]q was easily labeled with dye. Met1 in m[C]q was found to be removed by cell proteases, but its removal did not affect the reactivity of Cys2 with reagent. The dye coupling reaction was almost complete within two hours (Figure 35 A). In contrast, S65C could not be labeled without the aid of denaturant (Figure 35 B). When 4 M GdnHCl was added to the reaction mixture, the coupling yield of S65C was ≥ 76 %.

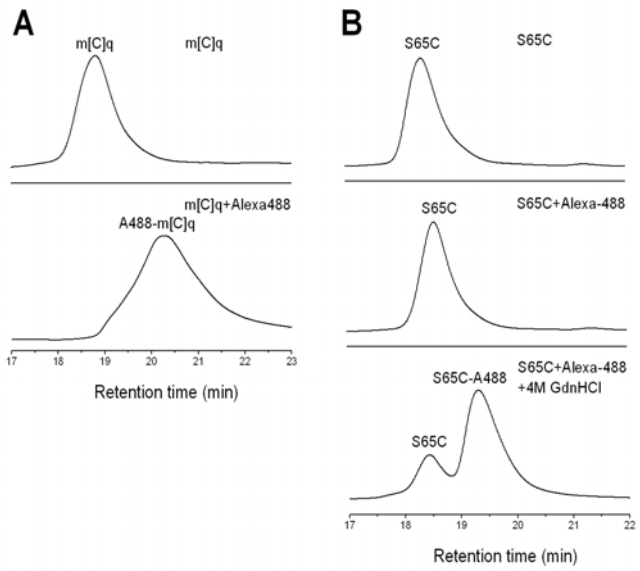

Figure 35. HPLC profiles of the dye coupling reactions of the proteins m[C]q (A) and S65C (B).

Hence, the double mutant protein m[C]q/S65C has Cys with different labelling activity. The donor dye, Alexa fluor 488 C5 maleimide (Alexa-488) (Molecular Probes Inc.), was labeled to the sulfhydryl group of the more reactive Cys, m[C]q, and the acceptor dye, Alexa fluor 594 C5 maleimide (Alexa-594) (Molecular Probes Inc.), was labeled to the sulfhydryl group of the less reactive Cys, S65C, in a partially denaturing condition. Using this strategy, dye conjugation is site-specific, and the double-labeled ubiquitin mutant protein is thus denoted as A488-m[C]q/S65C-A594 (Figure 14)

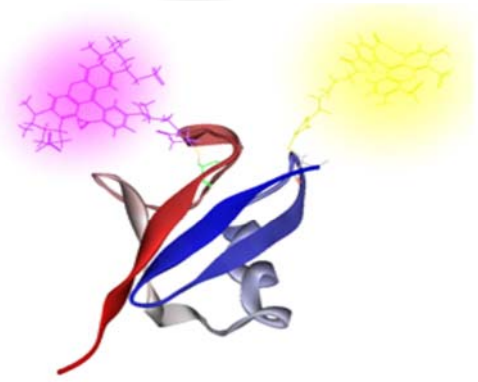

Figure 36. Schematic of doubly labelled ubiquitin, A488-m[C]q/S65C-A594. A488 and A594 are shown in yellow and pink, respectively.

4.3: Structural Characterization

For the sake of dye-labeling and purification, a histidine tag (formed by 6 histidines) and mutations, m[C]q and S65C, were introduced into native ubiquitin. The structures of the ubiquitin mutants with/without dye-labeling were characterized by circular dichrosim spectroscopy (Figure 37). In Figure 37, we could find that the secondary structures were intact in the native condition.

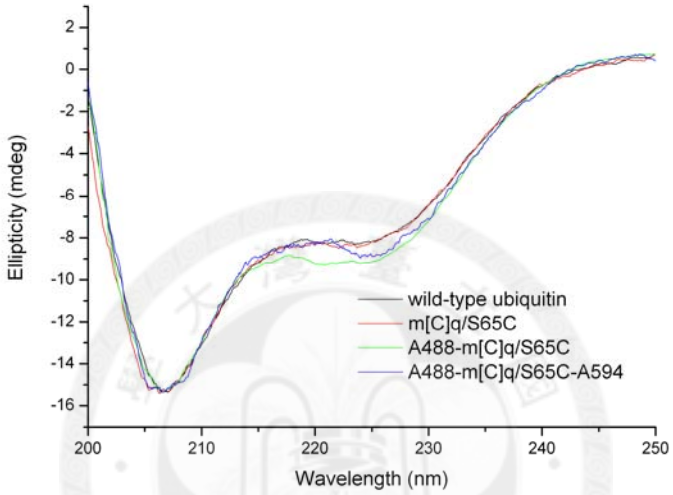

Figure 37. Circular dichroism spectra of wild-type ubiquitin, m[C]q/S65C, A488-m[C]q/S65C and A488-m[C]q/S65C-A594.

However, the stabilities were lowered by mutants and dyes (Figure 38). The chemical resistance of ubiquitin to GdnHCl was shifted to ~2.5 M due to the introducing dyes. According to the results of structural characterizations, we come to a conclusion that the mutated ubiquitin still has the same overall architecture but becomes less stable than the native one.

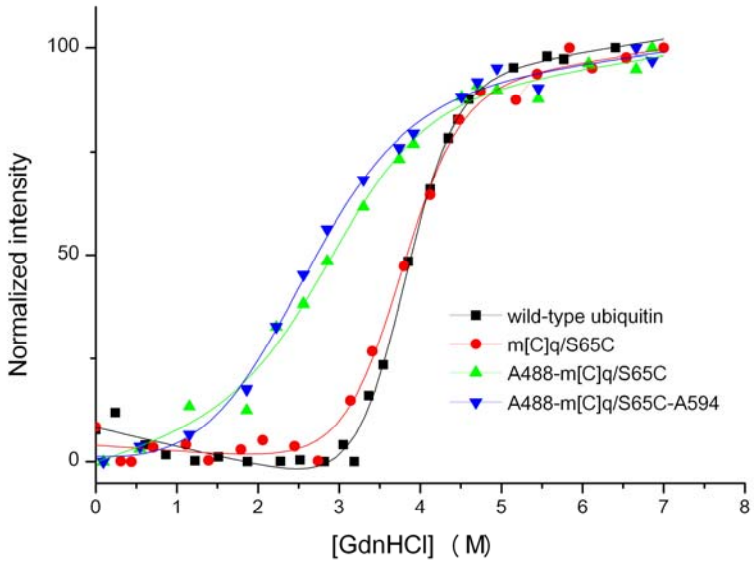

Figure 38. Chemical denaturation curves of ubiquitin (black), m[C]q/S65C (red), A488-m[C]q/S65C (green), and A488-m[C]q/S65C-A594 (blue) [77].

4.4: Observations on Ubiquitin by spFRET

Doubly labelled ubiquitin was provided by our collaborator, Dr. Rita P.-Y. Chen's lab in Institute of Biological Chemistry, Academia Sinica. With the help of FRET and confocal microscopy, we are able to investigate the intra-molecular distance change of a single protein molecule via fluorescence behaviours of donor and acceptor. To observe the dynamics of a single ubiquitin molecule, gel-immobilization was used to spatially confine protein molecules. On the other hand, we also performed experiments for protein in free solution to examine if the immobilization affects ubqiutin. Though the dynamics is not available since the passage time of a protein molecule through the detection focal volume is too fast to be resolved, the FRET histogram can still be obtained.

4.4.1: Surface Immobilization by Agarose gel

Experimental Setup

Single-molecule experiments were performed on a home-built scanning stage confocal microscope. An Argon/.16W laser (Spectra-Physics Lasers) provided excitation at 488 nm

which was reflected by a dichroic mirror and condensed by an objective (100X /1.3 NA oil, Nikon Inc.) to focus on the sample plate. Fluorescence emission was collected by the same objective, passing through a 500nm long pass filter (HQ500LP, Chroma Technology Corp.). Two different dichroic mirrors (Omega Inc.) which have cutting edges at 500 nm and 550 nm respectively were placed in the middle of optical path of fluorescence emission. The first one was to further eliminate excitation scattered light while the second one was to separate donor and acceptor emission. Fluorescence of Alexa Fluor 488 and 594 (Molecular Probes Inc.) was then collected by two photon-counting modules (SPCM-AQR-15-FC, PerkinElmer Optoelectronics) respectively. Two band-pass filters (HQ535/70 and BP60/60, Chroma Technology Corp.) were introduced in front of detectors for donor and acceptor channel respectively to eliminate laser excitation and spectral overlap.

To study dynamics of every single ubiquitin molecule, proteins are immobilized by 1 % agarose gel (Agarose, Low melting point, Sigma-Aldrich). The immobilization procedures are illustrated in Figure 39. 1 % agarose (Agarose, Low melting point, Sigma-Aldrich) was melted in 70 ℃ in water bath and cooled to 60 ℃ before use. Dye-labelled ubiquitin mutant, A488-m[C]q/S65C-A594, was dissolved in pure distilled water, mixed with the melted agarose to a final protein concentration ranging from 500 pM to 5 nM, and then spin-coated on a pre-coating cover glass with agarose gel as a buffer layer. This cover glass was inversely placed on the top of a concave glass slide, which was filled with the same agarose gel. To maintain humidity, the surrounding of the cover glass was sealed with nail polish. A series of dilution was performed to make sure single-molecule detection was achieved.

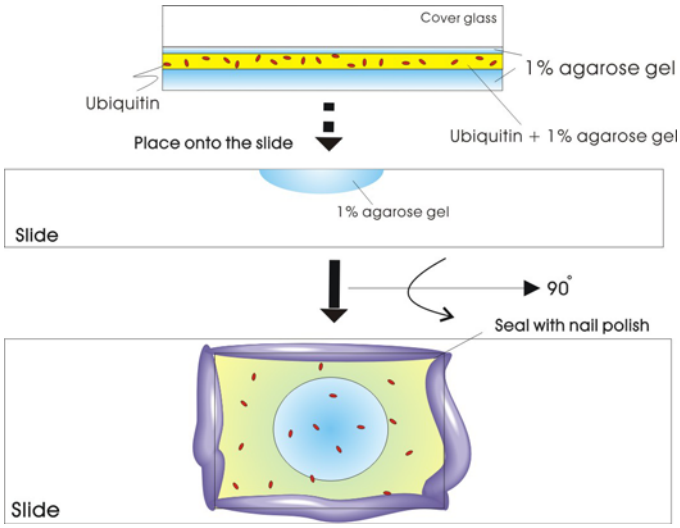

Figure 39. Illustration of gel-immobilization process.

Images Figure 40 obtained by confocal microscope were integrated by scanning with a three-axis piezo-scanning stage (P-517.3CL, Physik Instrumente GmbH & Co.) powered by the controller (E710.4CL, Physik Instrumente GmbH & Co.). The image-acquisition software was programmed in Labview. Each scanning step size is assigned to be 0.2 μm, and a diffraction limit spot comprises 3 to 5 pixels in general. Ubiquitin molecules, m[C]q/S65C, have donor and acceptor dye molecules labelled specifically on the end of β 1 and β 5 strand, respectively. Structural variations concerning the core of ubiquitin can be projected in terms of energy transfer efficiency of FRET since the β 1 and β 5 strand are involved in. The distance between donor (Alexa 488) and acceptor (Alexa 594) was evaluated by the software, Discovery Studio 2.0, and the value is ~ 38 Å, which corresponds to ~ 95 % FRET efficiency on the basis of R_0 = 60Å.

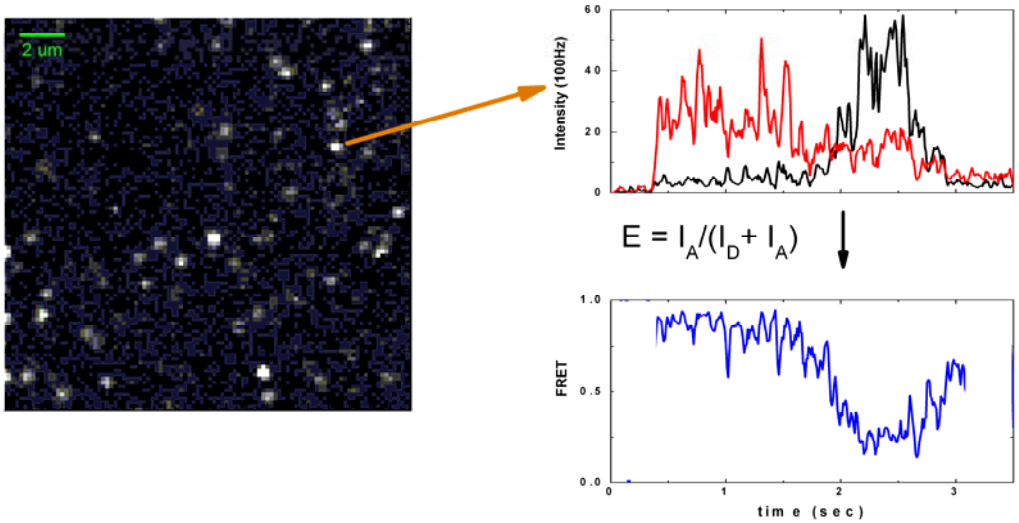

Figure 40. Confocal image (20 μm X 20 μm) of immobilized ubiquitin molecules; the time trajectory and its corresponding FRET.

spFRET in Free Solution

For experiments in free solution, the confocal spot was directly focused into sample solutions by 25 – 30 um. As the concentration goes down to 100 pM -1 nM, distinguished fluorescence bursts corresponding to single molecules swimming through the focused laser spot could be observed. A solution chamber was confined by a commercial double-side sticker, Gene Frame (Thermo Scientific Inc.), and sample volume was 25 ul. Both glass cover-slips and substrates were pre-cleaned and exposed to UV ozone for 30 minutes before use. Surfactant, 0.001 % (v/v) Tween 20, was used to prevent surface denaturation; 5 - 10 mM DABCO was added into solution to prolong the chemical durations of dye molecules.

FRET Data Analysis

The FRET efficiency E_{ET} was calculated according to Equation (38), where I_D and I_A are the donor and acceptor emission intensity after subtracting their individual background; γ is the correcting factor for the difference of detection efficiency of two APDs; α is the spectral leakage ratio from donor to acceptor channel. γ was measured from the ratio of emission of thick-filmed conjugated polymers MEH-PPV, which has broad spectrum covering from 500 nm to ~ 700 nm, in donor and acceptor channel, and the value we obtained was 0.879. α was measured as the acceptor/donor intensity ratio for the donor-only sample, A488-m[C]q/S65C, and the value obtained was 0.02455. Each

intensity time trajectory of a detected molecule lasted 10 sec to make sure of donor/acceptor being photobleached; and the time bin was set as 10 ms. Intensity thresholds were imposed on donor and acceptor channel to select signals out of background noises. The fluorescence signals per time bin which had the intensity higher than the threshold (Equation (38) counts for either donor or acceptor channel) were selected, and were converted into FRET efficiency. The behaviour of each molecule was normalized according to its chemical duration time to construct its sub-FRET histogram. Therefore, the area of each sub-FRET histogram was fixed as one, and the overall FRET histogram was constructed by summing up the sub-FRET histograms of all molecules [14]. In addition, molecules were further categorized manually [78] according to their features: (i) High FRET : FRET > 50 %; (ii) Low FRET : FRET < 50 %; (iii) Switching : Emission of donor and acceptor changes anti-correlatively [79].

$$E \equiv \frac{I_A}{I_A + I_D} = \frac{I_A - \gamma \cdot \alpha \cdot I_D}{I_A + (1 - \gamma \cdot \alpha) \cdot I_D} \tag{38}$$

4.5: Results, Discussion & Conclusion

The structures of the mutant protein, m[C]q/S65C, before and after dye-labeling were compared with the wild-type ubiquitin by using circular dichroism spectroscopy. Basically, the overall ubiquitin architecture was not affected by the mutations or dye-labeling. However, while the structural stability of m[C]q/S65C was the same as wild-type ubiquitin, the chemical stability of A488-m[C]q/S65C-A594 was substantially decreased after first dye-labeling. The free energy change (ΔG^{H2O}) of ubiquitin, m[C]q/S65C, A488-m[C]q/S65C, and A488-m[C]q/S65C-A594 derived from the chemical denaturation curves are -7.1 ± 0.6 kcal/mol, -6.1 ± 0.8 kcal/mol, -3.0 ± 1.2 kcal/mol and -2.2 ± 0.6 kcal/mol, respectively. Previously the influence of dye-labeling in FRET studies had hardly been well examined. The difference of the folding free energy change ($\Delta\Delta G^{H2O}$) of ubiquitin after dye-labeling is as big as 4.9 kcal/mol. The refolding rate of A488-m[C]q/S65C-A594 is the same as the wildtype ubiquitin [80], suggesting that dye-labeling did not affect the

energy gap between the unfolded state and the transition state but destabilize the native state. Moreover, single dye-addition was enough to destabilize the protein.

4.5.1: Conformational Heterogeneity of A488-m[C]q/S65C-A594

According to the FRET histogram constructed from 221 molecules, heterogeneity was observed in the FRET efficiency histograms (Figure 41D). That might be resulted from several reasons, and we will discuss over them in this section.

Figure 41 (A) and (B) are the intensity trajectories of two cases with high FRET efficiency. From their sub-FRET histograms, it is obvious that the FRET histogram is peaked at either 72 % (or 95 %) and ~ 0% which is attributed to acceptor photobleaching. On the other hand, we can see some molecules exhibiting low FRET efficiency as well (Figure 41 C). The final FRET histogram of 221 molecules is shown in Figure 19D, and it can be decomposed into four sub-states by fitting to 4 Gaussian distributions (Equation (39)): 3 % (donor only); 22 % (low FRET); 72 % (middle FRET) and 95 % (high FRET). The zero-peak centering at E = 3 % corresponds to either the donor-only proteins or the process of photobleaching acceptors [81]. The distance between two labeled dyes is estimated to be ~ 38 Å in native structure of ubiquitin, and the corresponding FRET efficiency should be 94 % under the assumption of R_0 = 60 Å. This might imply that the high FRET state (95 %) is attributed to the native-like structure of ubiquitin. However, the existence of low FRET state (22 %) and middle FRET one (72 %) is very interesting, especially transitions among states are also observed as well. The sub-FRET trajectories in Figure 19 (A), (B) and (C) provide us with additional information concerning the conformational flexibility of high FRET (95 %), middle FRET (72 %) and low FRET (22 %) state. The FWHM of sub-FRET distribution of middle FRET (48.3 %) is broader than that of low FRET (20.0 %) and high FRET (17.7 %).

$$y = \sum_{i=1}^{4} \frac{A_i}{W_i \cdot \sqrt{\pi/2}} \cdot \exp\left(-2 \cdot \left(\frac{x - x_i}{W_i} \right)^2 \right)$$
$$FWHM = \sqrt{2 \cdot \ln 2} \cdot W = 1.1774 * W \qquad (39)$$

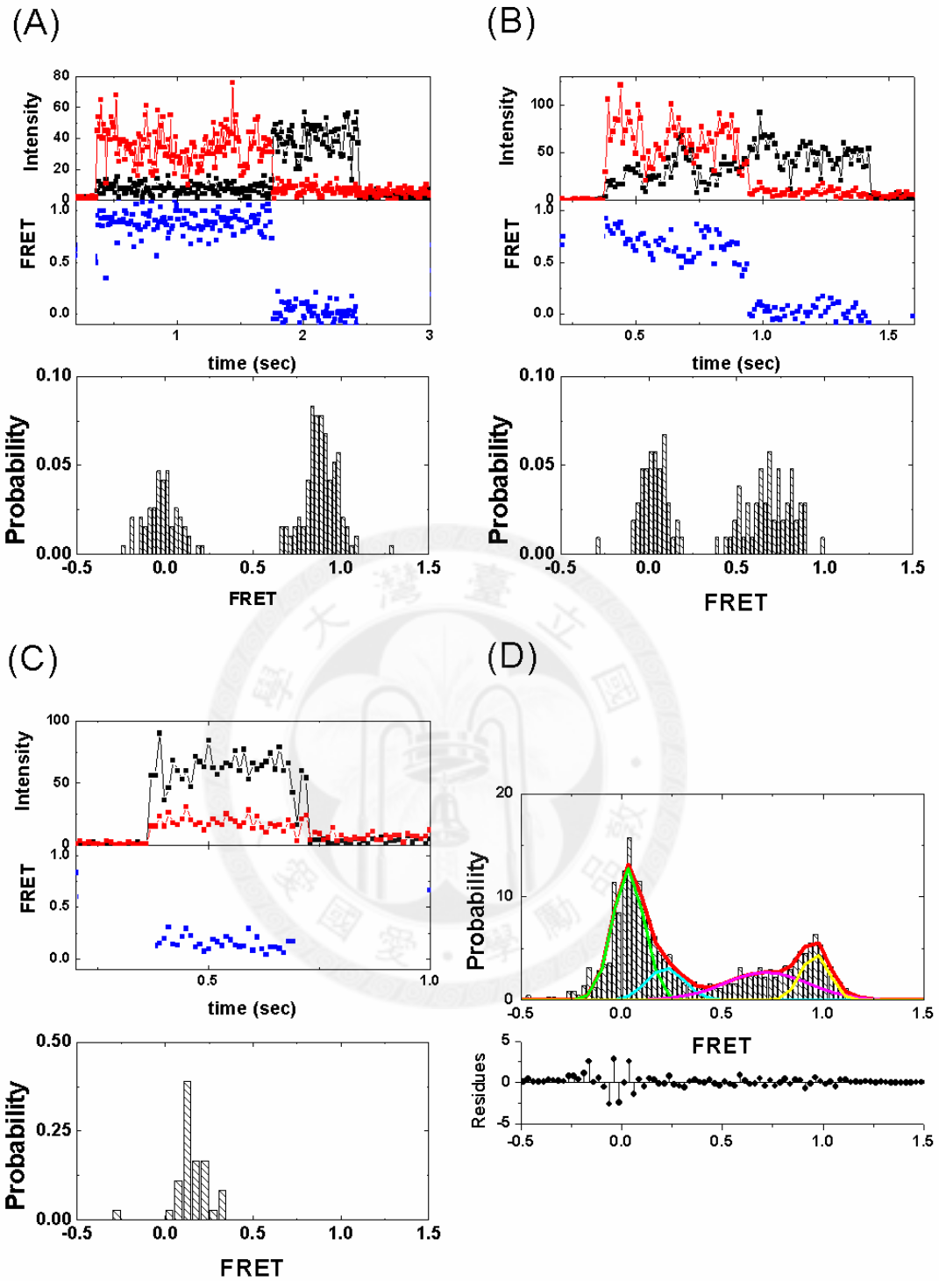

Figure 41. Time trajectory, the corresponding FRET efficiency and FRET efficiency histogram of ubiquitin molecules at FRET efficiency (A) ~ 95 %, (B) ~ 70 % and (C) 20 %. (D) are the final FRET histogram by accumulating 222 ubiquitin molecules and its fitting curves with residues (Black – Donor emission; Red – Acceptor emission) .

. In addition to the peak values of distributions of FRET histograms, the widths of different populations could provide with information regarding the conformational flexibility. Nevertheless, the distribution broadening-up can also arise from other factors, that is shot noises from background, transitions to dark states, dipole reorientation and spectral diffusion [6]

Assuming that the photon statistics obeys Poisson distribution, the expected standard deviation of spFRET [82] can be estimated with donor and acceptor intensities, Equation (40) [83]. The total count rate is at least 20 counts per time bin (10 ms) since the thresholds are imposed to construct FRET histograms. The expected FWHM (Full Width Half Maximum) calculated from the estimate standard deviation (σ_{FRET}) ranges from 11.5 % (at E = 4.5 %) to 26.2 % (at E = 50 %), Figure 42. The FWHM obtained from FRET histogram of donor-only molecules, 15.3 %, is comparable to the estimated value. Therefore, the FWHM of donor-only molecules can be adopted as the precision of our spFRET system. The FWHM of low and high FRET state are both comparable to that of our system. Though they are slightly broader than the expected FWHM, their structures should still be regarded as definite ones since the contribution of shot noise to the distribution width is neglected. Yet, the middle FRET state (72 %) has a quite broad distribution (48.3 %), which suggests the existence of an intermediate which has loosely-packed structure relative to the native-like one.

$$\sigma_{FRET} = \sqrt{\frac{E \cdot (1-E)}{I_a + I_d}} \tag{40}$$

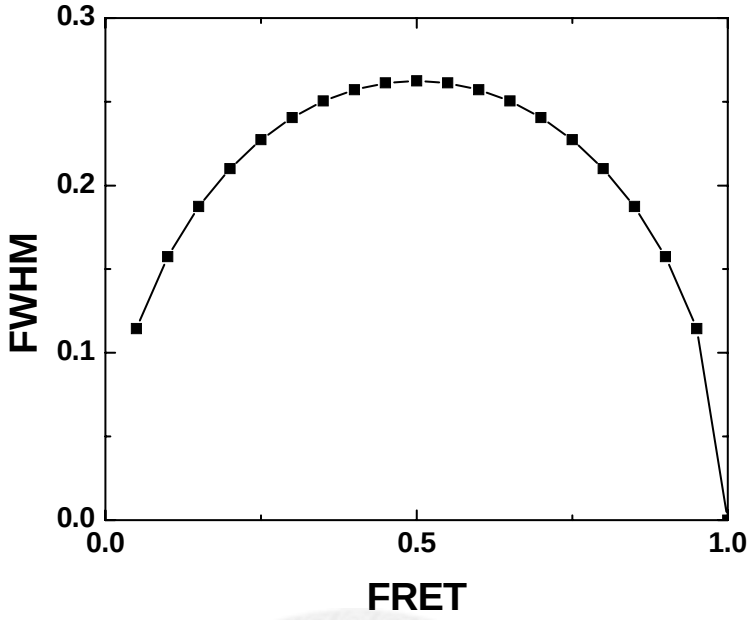

Figure 42. Estimated precision of FRET based on Poisson statistics.

4.5.2: Structural Switching

The intermediate might play a role in mediating ubiquitin molecules between its native and the unfolded one. Transitions between the middle FRET state and high FRET state were observed, Figure 43 (A) while a slower donor and acceptor intensity swapping process between high FRET and low FRET state is shown in Figure 43 (B). After accumulating 46 ubiquitin molecules revealing intensity "switching" between donor and acceptor, the FRET histogram for this category is constructed (Figure 43C). The FRET distribution comprises 4 Gaussian distributions as well (Equation (39)), and the zero-peak is attributed to acceptor photobleaching which is also counted in.

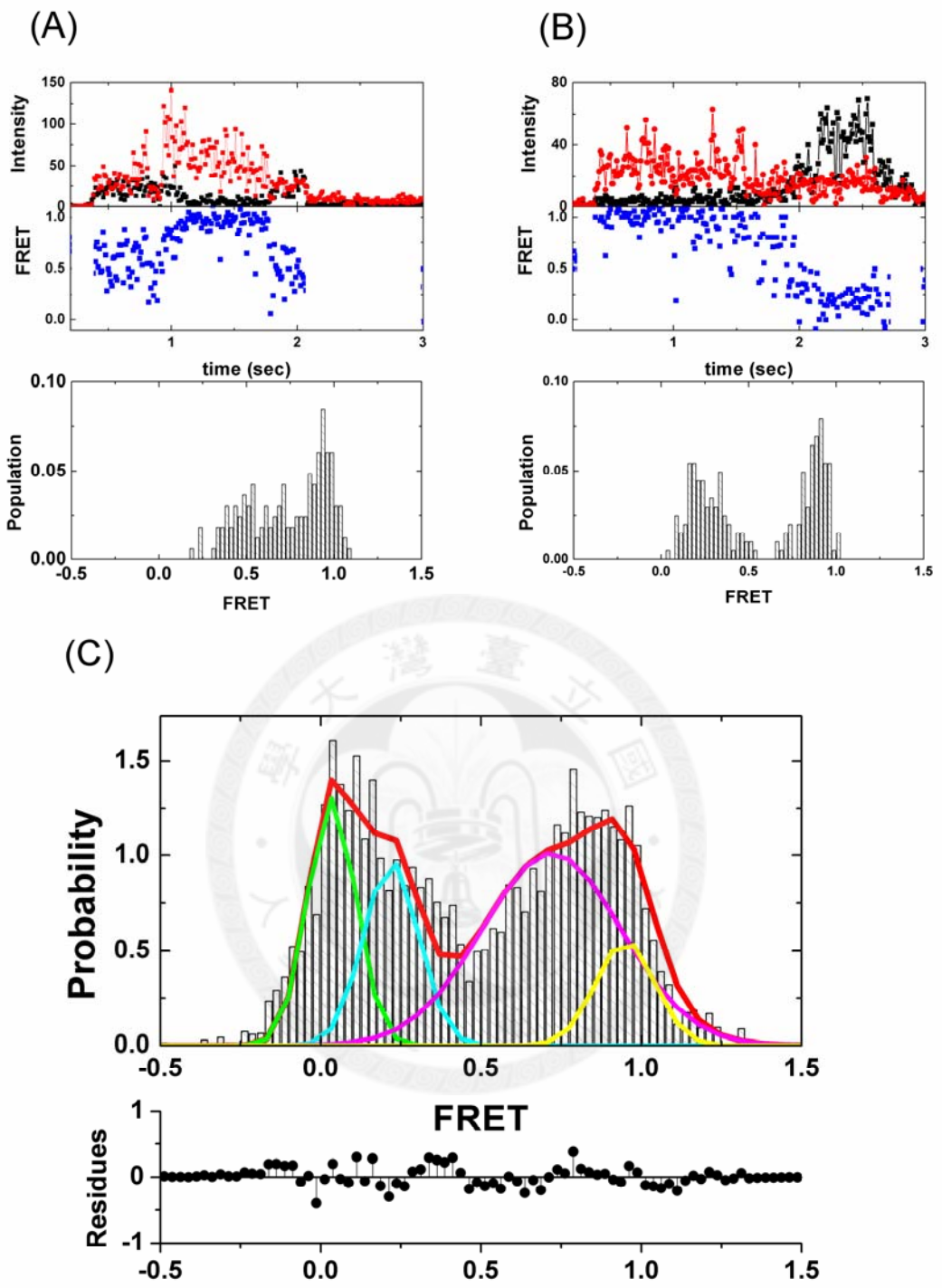

Figure 43. The intensity trajectories and the corresponding FRET efficiency distributions of ubiquitin molecules revealing intensity "switching" behavior. (Black – Donor emission; Red – Acceptor emission) (A) and (B) are trajectories showing different intensity swapping tendency. (A) is the transition from Middle FRET (72 %) to High FRET (95 %) and then go back to Middle FRET (72 %) state; (B) is slowly swapping from Low FRET (22 %) to High FRET (95 %) state. (C) is the final FRET efficiency histograms by accumulating 46 ubiquitin molecules which present intensity switching and its fitting curves with residues.

4.5.3: Effects of Swapping Positions of spFRET pair

Our protein-dye labeling method enables us to swap the dye labeling positions easily, and how the swap FRET pairs affects proteins is less explored in other protein-dye labeling methods [77]. When Alexa-594 was added to m[C]q/S65C before Alexa-488, the produced protein, denoted A594-m[C]q/S65C-A488, was compared with A488-m[C]q/S65C-A594. The protein solubility of A594-m[C]/qS65C-A488 was much poorer than that of A488-m[C]q/S65C-A594. On the other hand, FRET distributions constructed from freely diffusing single-molecule experiments also reveal the intrinsic differences resulted from the swap of two dye molecules. For A488-m[C]q/S65C-A594, a hump locating at 80% was observed while two humps appeared in the case of A594-m[C]q/S65C-A488 (Figure 22). The results showed that swapping donor and acceptor dye molecules affected FRET distributions. For A594-m[C]q/S65C-A488, nearly half of molecules were populated in higher FRET region while the rest were in the lower one. Nevertheless, most of molecules of A488-m[C]q/S65C-A594 had FRET efficiencies higher than 50%.

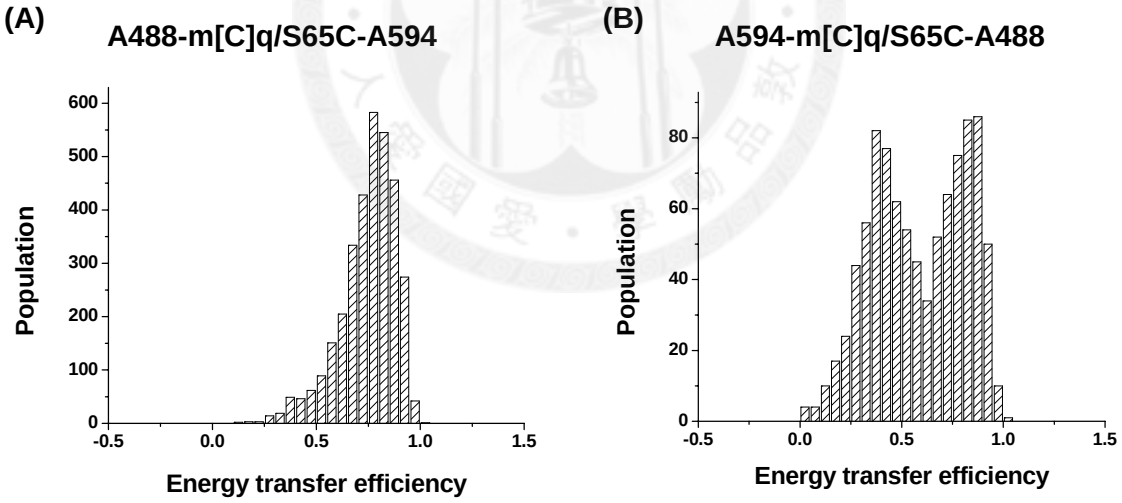

Figure 44. Freely diffusing single-molecule experiments of (A) A488-m[C]q/S65C-A594 and (B) A594-m[C]q/S65C-A488.

In addition, solvent effects on spFRET ubiquitin molecules were found by the excitation spectrum in Figure 23. The excitation spectrum monitoring at 620nm (acceptor) can qualitatively reveal how different excitation wavelengths contribute to emission at 620nm

(acceptor), and the peak at 488nm corresponds to contributions from FRET. In the presence of 0.001% Tween and 5mM DABCO, Alexa 488 and 594 were brighter, and A488-m[C]q/S65C-A594 had higher/more FRET efficiency/events in average. Oppositely, in pure water A594-m[C]q/S65C-A488 had slightly higher/more FRET efficiency/events instead. .

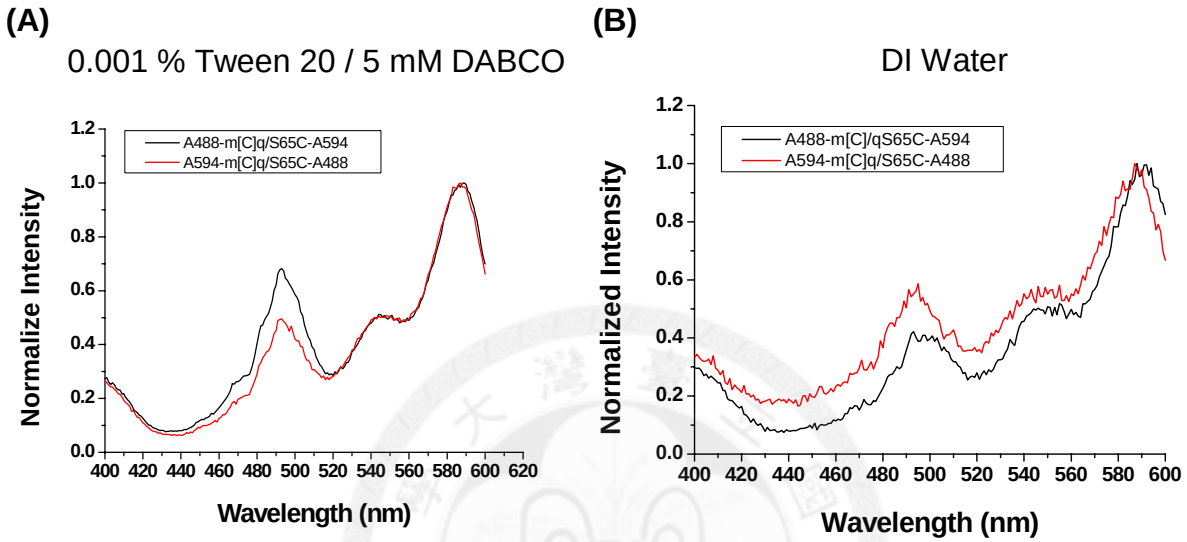

Figure 45. Excitation spectrum at 620nm of A594-m[C]q/S65C-A488 and A488-m[C]q/S65C-A594 in (A) 0.001% Tween20 + 5mM DABCO and (B) DI water. (Black : A488 - m[C]q/S65C - A594; Red : A594 - m[C]q/S65C - A488)

Our observations on the effect of swapping FRET pair position further suggested the interactions between dye molecules and proteins, which was less addressed in spFRET study on proteins.

4.5.4: Issues on Dye Molecules

Stability of Alexa Flour 594

Comparison among emission spectrum of A488-m[C]q/S65C-A594 from the same batch taken on different date was made. It was found that the peak intensity ratio, I_D/I_A, decreased with time (Figure 24B), which might be due to either decrease on FRET efficiency or less FRET events occurring

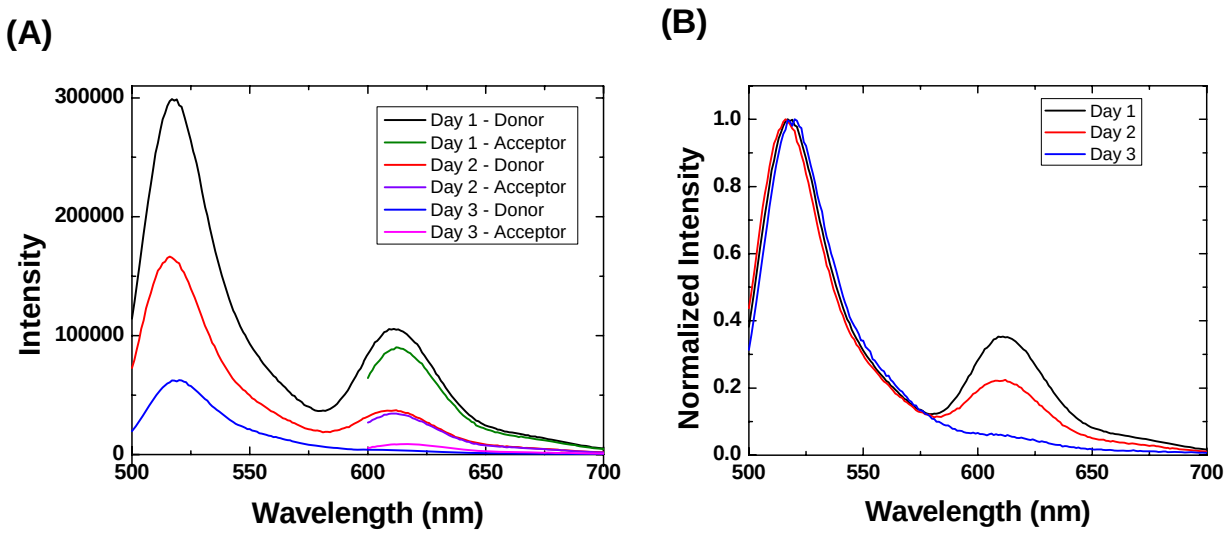

Figure 46. (A) Emission spectrum of A488-m[C]q/S65C-A594 of different dyes at 488 nm and 594 nm respectively. (B) Comparison of emission spectrum normalized by the intensity at 520 nm.

Interestingly, the fluorescence emission of Alexa Fluor 594 also decreased in the same manner (Figure 24A), which suggested the issue of the stability of Alexa Fluor 594. There are a variety of interactions within proteins, namely electrostatic forces and hydrophobic interactions, which makes proteins versatile and flexible. However, dye molecules are sensitive to its surroundings, and slightly changes in its local environments could lead to changes in its properties [84]. Thus, dye-labeling on ubiquitin might destabilize ubqiutin itself and vice versa. Furthermore, interactions between dyes and proteins are unique and case-dependent.

Dipole Re-orientation

The relative rotational flexibility of donor and acceptor emission/absorption dipole could strongly affect the förster resonance energy transfer efficiency (E_{ET}) irrespective to the distance between the FRET pair. To examine the relative rotational flexibility of the dipole of dye molecules, measurements of time-resolved fluorescence anisotropy was adopted. Anisotropy, *r(t)*, of fluorescence is defined as Equation (41), and is dependent on the rotational diffusion of the observed species.

$$r(t) = \frac{I_{VV} - I_{VH}}{I_{VV} + 2 \cdot I_{VH}} \tag{41}$$

Where, I_{VV} is the polarization of emission parallel to that of excitation, and I_{VH} stands for the emission polarization perpendicular to the excitation. Generally, the anisotropy relaxation follows the trend of exponential decays, and θ is the rotational diffusion coefficient.

$$r(t) = \sum_i r_{0_i} \cdot \exp\left(-\frac{t}{\theta_i}\right) \tag{42}$$

When there are more than one species, the final anisotropy relaxation curve is the sum over all the species (Equation (42)). For a protein with 10 kD in molecular weight, the rotational correlation time is around 3 ~ 5 ns at room temperature.

We compared the anisotropy relaxations of pure donor dye molecules, Alexa Fluor 488, and donor-labeled ubqiutin mutant, m[C]q-A488 (Figure 47). The excitation was generally by Ti:sapphire Laser (Coherent, Mira 900) and a second harmonic generator at 460 nm with the repetition rate of 76 MHz. The emission parallel and perpendicular to the excitation was collected respectively, and the anisotropy was calculated according to Equation (41).

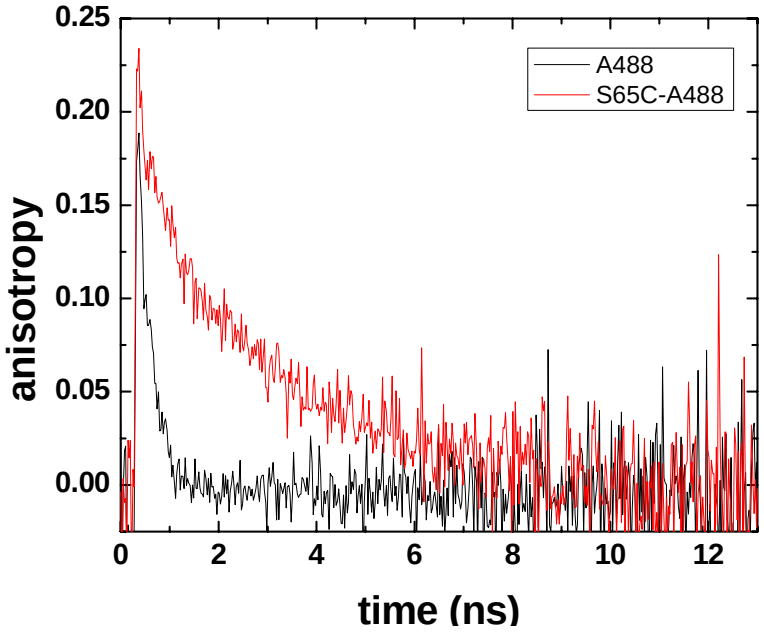

Figure 47. Time-resolved fluorescence anisotropy of pure donor dye molecule, Alexa Fluor 488, and S65C-A488.

The anisotropy decay curves S65C-A488 has a slower relaxation process (3.6 ns) and a fast phase (400 ps) at the very beginning. On the other hand, the anisotropy relaxation of A488 was fitted by a single exponential decay (300 ps). The fast correlation time (~ 300-400 ps) was assigned to the rotational diffusion of dye molecules while the slower phase was attributed to the rotation of protein molecule with dye. This observation implied that the attached dye molecule was relatively free from the target protein instead of aligning on the surface or being trapped at a certain angle.

4.5.5: Concluding Remarks

From our investigation on the ubiquitin mutant, m[C]q/S65C, we conclude that it was destabilized after dye-labeling. On the other hand, the heterogeneous distributions of conformation were also observed in spFRET experiments, and ubiquitin molecules were populated in three different states except the zero-peak distribution. A possible origin responsible for the FRET heterogeneity is the effect of dipole re-orientation. However, the result of time-resolved fluorescence anisotropy measurements on A488 and m[C]q-A488 had proved the rotational flexibility of dyes. Our explanations to the observed phenomenon is that ubiquitin was driven out of the native state in the energy landscape due

to mutations and further stabilized by the hydrophobic interactions from dye molecules. The branch at high-FRET state (E_{ET} = 95 %) was more native-like according to the distance derived from FRET efficiency while that of low-FRET state (E_{ET} = 22 %) had a huge difference in the distance and was likely to be an unfolded one. In between of the native-like and unfolded state, a population centering at E_{ET} = 72 % with a broader width appeared. It implied the existence of the dynamic tertiary structure of ubiquitin mutant, and the middle-FRET state (E_{ET} = 72 %) could be views as a molten globule intermediate. The mutation and dye-labeling in our research acts as a mildly denaturing condition, and a dynamic intermediate is stabilized to observe. It is generally believed that a protein folds through progressively more structured intermediates to acquire its unique three dimensional structure [85, 86], and a molten globule intermediate is slightly higher than the native one in terms of energy. Observations on the conformational properties of the molten globule intermediate of ubiquitin via spFRET would provide valuable information about the study of protein folding pathway.

CHAPTER 5

CONCLUSIONS & Perspective

5.1: Conclusions

A set of optical methods to investigate fluorescence emission and its fluctuations have been established. The study of conformation of ubiquitin via spFRET, and characterizations of various fluorescence objects (FNDs, microspheres and conjugated polymers) are presented and discussed. Single-molecule spectroscopy provides local insights into the structure, dynamics and population heterogeneity of biomolecules. Among those interesting molecules, we are most fascinated with proteins for its role in biological systems. The relation between structure (dynamics) and function, protein folding / unfolding processes, and molecular recognitions are the possible future topics.

The nature of protein molecules, being marginally stable and high sensitivity, makes protein flexible but fragile [87]. Mutations, solvents and dye-labeling could extrinsically affect the protein molecule, which makes the detection even more difficult. Optical detection is known for its non-intrusive nature, and has been widely applied to the studies on biological systems at molecular level. However, the interplay between biomolecules and dye molecules is still an open question. In view of this intrinsic limitation of using dyes as probes for conformation, we try to collect additional information via correlation and single-photon counting technique, and hope to gain the deeper understanding.

In addition to the reasons mentioned above, fluorescence correlation spectroscopy (FCS) is also indispensable in the study of kinetics on micro-fluidics. On the one hand, the flow (traveling) velocity is paramount for the sake of precision of time resolution. On the other hand, it is difficult to stare at one molecule and records its intensity variation with time in free solution (flow), and some dynamics information might be lost. FCS provides both the information regarding velocity and other origins contributing to fluorescence fluctuations (i.e. structural dynamics). All these efforts are actually the preparations for the research on protein folding / unfolding study at single molecule level or ensemble [50, 58, 59, 88, 89].

5.2: Perspective

The spectroscopic probes including circular dichroism, FRET [84, 90], time-correlated single photon counting (TCSPC) and SAXS (small angle X-ray scattering) [89, 91-93] provide the local and global structural information of molecules. The most prominent advantage of the spectroscopic probes is their compatibilities with the measurements in kinetic processes of biomolecules.

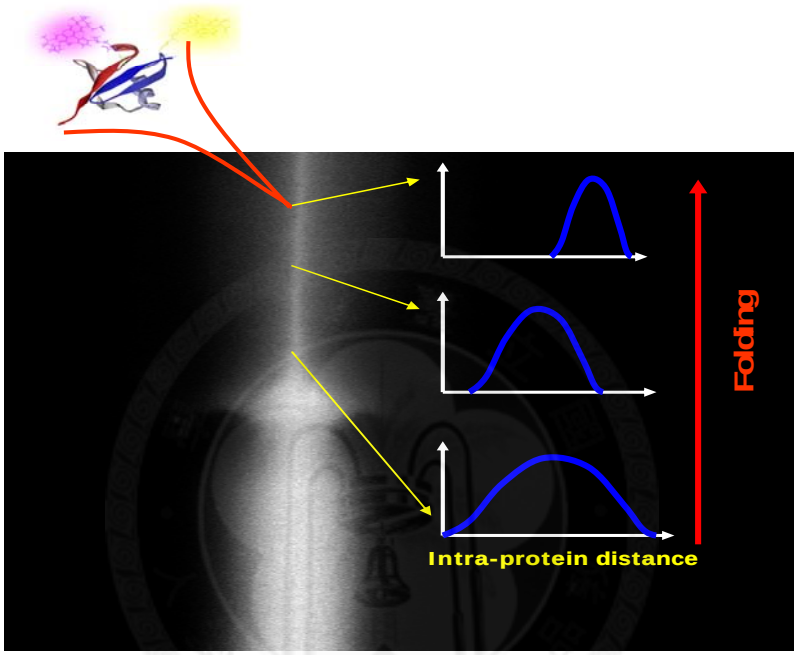

Figure 48. Combination of FRET and micro-fluidics.

A micro-fabricated continuous-flow mixer has the superior benefits on the sample consumption rate and the observation time duration. Since the time evolution is transformed into the position in space in terms of flow velocity (Figure 48), the kinetic process at certain time point can be investigated for longer time. By combining microfluidic mixing device with FCS, TCSPC and FRET, population heterogeneities and transitions between populations could be obtained at every stage along the folding/unfolding path.

BIBLIOGRAPHY

1. Moerner, W.E. and L. Kador, *Optical detection and spectroscopy of single molecules in a solid.* Physical Review Letters, 1989. **62**(21): p. 2535.
2. Weiss, S., *Fluorescence Spectroscopy of Single Biomolecules.* Science, 1999. **283**(5408): p. 1676-1683.
3. R. Rigler, M.O.a.I.B., *Single Molecule Spectroscopy - Nobel Conference Lectues*. 2001: Springer.
4. Adachi, K., et al., *Stepping rotation of F1-ATPase visualized through angle-resolved single-fluorophore imaging.* Proceedings of the National Academy of Sciences of the United States of America, 2000. **97**(13): p. 7243-7247.
5. Zhuang, X., et al., *Correlating Structural Dynamics and Function in Single Ribozyme Molecules.* Science, 2002. **296**(5572): p. 1473-1476.
6. Ha, T., et al., *Single-molecule fluorescence spectroscopy of enzyme conformational dynamics and cleavage mechanism.* Proceedings of the National Academy of Sciences of the United States of America, 1999. **96**(3): p. 893-898.
7. Michel, O., *Photon Statistics in Single Molecule Experiments.* Single Molecule, 2002. **3**(5-6): p. 255-265.
8. Orrit, M., *Single-molecule spectroscopy: The road ahead.* The Journal of Chemical Physics, 2002. **117**(24): p. 10938-10946.
9. Markus Lippitz, F.K.M.O., *Statistical Evaluation of Single Nano-Object Fluorescence.* Chem Phys Chem, 2005. **6**(5): p. 770-789.
10. Copy right belongs to Nikon Microscope U.
11. Copy right belongs to Nikon Microscope U.
12. Copy right belongs to Nikon Microscope U.
13. T, F., *Zwischenmolekulare Energiewanderung und Fluoreszenz.* Annalen der Physik, 1948. **2**(6): p. 55-74.
14. Hanson, J.A., et al., *Illuminating the mechanistic roles of enzyme conformational dynamics.* Proceedings of the National Academy of Sciences of the United States of America, 2007. **104** (46): p. 18055-18060.
15. Xie, Z., et al., *Single-molecule studies highlight conformational heterogeneity in the early folding steps of a large ribozyme.* Proceedings of the National Academy of Sciences of the United States of America, 2004. **101**(2): p. 534-539.
16. The energy transfer mechanism of FRET does not have radiative process involved though spectrum of dyes are essentail to determine the forster radius of a chosen dye pair.
17. Wiener, N., *Extrapolation, interpolation and smoothing of stationary time series.* MIT Press, 1949.
18. Magde, D., E. Elson, and W.W. Webb, *Thermodynamic Fluctuations in a Reacting System - Measurement by Fluorescence Correlation Spectroscopy.* Physical Review Letters, 1972. **29**(11): p. 705.
19. Elliot L. Elson, D.M., *Fluorescence correlation spectroscopy. I. Conceptual basis and theory.* Biopolymers, 1974. **13**: p. 1-27.
20. Douglas Magde, E.L.E., Watt W. Webb, *Fluorescence correlation spectroscopy. II. An experimental realization.* Biopolymers, 1974. **13**: p. 29-61.
21. Jerker Widengren, R.R.a.Ü.M., *Triplet-state monitoring by fluorescence correlation spectroscopy.* Journal of Fluorescence, 1994. **4**(3): p. 255-258.

22. Widergren, R.R.a.J., *Ultrasensitive detection of single moleculres by fluorescence correlation spectroscopy.* BioScience, 1990. **3**: p. 180-183.
23. Rigler, Ü.M.a.R., *Submillisecond detection of single rhodamine molecules in water.* Journal of Fluorescence, 1994. **4** (3): p. 259-264.
24. Dephasing time (T2 time) is on the order of 100 fs.
25. Biophysical Society, Educational Resourceshttp://www.biophysics.org/education/schwille.pdf
26. Schubert, M., et al., P*hoton antibunching and non-Poissonian fluorescence of a single three-level ion.* Physical Review Letters, 1992. **68** (20): p. 3016.
27. Twiss, R.H.a.R.Q., Nature, 1956. **177:** p. 27.
28. Biophysical Society, Educational Resourceshttp://www.biophysics.org/education/schwille.pdf
29. Laurence, T.A., et al., Ph*oton Arrival-Time Interval Distribution (PAID): A Novel Tool for Analyzing Molecular Interactions.* 2004. **108** p. 3051-3067.
30. Basch, T., et al., Ph*oton antibunching in the fluorescence of a single dye molecule trapped in a solid. P*hysical Review Letters, 1992. **69** (10): p. 1516.
31. Paul C. Brister, K.K.K., Volker Buschmann and Kenneth D. Weston, Fl*uorescence correlation spectroscopy for flow rate imaging and monitoring-optimization, limitations and artifacts. L*ab on a chip, 2005. **5**: p. 785-791.
32. Bernard, J., et al., Ph*oton bunching in the fluorescence from single molecules: A probe for intersystem crossing. T*he Journal of Chemical Physics, 1993. **98** (2): p. 850-859.
33. Zumbusch, A., et al., Pr*obing individual two-level systems in a polymer by correlation of single molecule fluorescence. P*hysical Review Letters, 1993. **70** (23): p. 3584.
34. Kulzer, F. and M. Orrit, SI*NGLE-MOLECULE OPTICS. A*nnual Review of Physical Chemistry, 2004. **55** (1): p. 585-611.
35. Moerner, W.E., Science, 1997. **277:** p. 1059.
36. Rasnik, I., S.A. McKinney, and T. Ha, *Nonblinking and long-lasting single-molecule fluorescence imaging. N*at Meth, 2006. **3** (11): p. 891-893.
37. Grewer, C. and H.D. Brauer, Me*chanism of the Triplet-State Quenching by Molecular-Oxygen in Solution. J*ournal of Physical Chemistry, 1994. **98** (16): p. 4230-4235.
38. Aitken, C.E., R.A. Marshall, and J.D. Puglisi, An *Oxygen Scavenging System for Improvement of Dye Stability in Single-Molecule Fluorescence Experiments. B*iophysical Journal, 2008. **94**(5): p. 1826-1835.
39. Xiangyun, Q., et al., Me*asuring Inter-DNA Potentials in Solution. P*hysical Review letters, 2006. **96** (13): p. 138101.
40. Holt, K.B., Phil. Trans. R. Soc. A, 2007. **65:** p. 2845-2861.
41. Y.-R. Chang, H.-Y.L., K. Chen, C.-C. Chang, D.-S. Tsai, C.-C. Fu,T.-S. Lim, Y.-K. Tzeng, C.-Y. Fang, C.-C. Han, H.-C. Chang, W. Fann, Nature Nanotech, 2008. **3**: p. 284-288.
42. S.-J. Yu, M.W.L., H.-C. Chang, K.-M. Chen, Y.-C. Yu, J. Am. Chem. Soc., 2005 **127**: p. 17604-17065.
43. C.-C. Fu, H.-Y. Lee,K. Chen, T.-S. Lim, H.-Y. Wu, P.-K. Lin, P.-K. Wei, P.-H. Tsao, H.-C. Chang, W. Fann, Proc. Natl. Acad. Sci. USA, 2007. **104:** p. 727-732.
44. Heikal, A.A., et al., Mo*lecular spectroscopy and dynamics of intrinsically fluorescent proteins: Coral red (dsRed) and yellow (Citrine). P*roceedings of the National Academy of Sciences, 2000. **97** (22): p. 11996-12001.

45. H. Qian, M.P.S., E.L. Elson, Si*ngle particle tracking. Analysis of diffusion and flow in two-dimensional systems Bi*ophysical Journal, 1991. **60** (4): p. 910-921.
46. According to the Einstein-Stokes relation, the diffusivity is closely related to the diameter of particles. However, its shape will aslo affect the diffusivity, which is beyone the scope of our discussion.
47. Knight, J.B., et al., Hy*drodynamic Focusing on a Silicon Chip: Mixing Nanoliters in Microseconds. P*hysical Review Letters, 1998. **80** (17): p. 3863.
48. David E. Hertzog, X.M., Marcus Jager, Xiangxu Kong, Juan G. Santiago, Shimon Weiss, and Olgica Bakajin, Fe*mtomole mixer for microsecond kinetics studies of protein folding. A*nal. Chem., 2004. **76:** p. 7169-7178.
49. Hye Yoon Park, X.Q., Elizabeth Rhoades, Jonas Korlach, Lias W. Kwok, Warren R. Zipfel, Watt W. Webb, and Lois Pollack, Ac*hieving uniform mixing in a microfluidic devices : Hydrodynamic Focusing Prior to Mixing. A*nal. Chem., 2006. **78:** p. 4465-4473.
50. Lipman, E.A., et al., Si*ngle-molecule measurement of protein folding kinetics. S*cience, 2003. **301** (5637): p. 1233-1235.
51. Yang, L.-L., Se*tup of an UltraFast Mixing Laminar Micro-fluidics for Protein Folding Study,* in Ph*ysics Department.* 2003, National Taiwan University: Taipei. p. 97.
52. (劉慶川), C.-C.Liu., In*vestigations on Hydrodynamic Focusing by Con-focal Microscopy and Fluorescence Correlation Spectroscopy (共焦顯微鏡與螢光相關光譜分析於微流體聚焦之研究),* in In*stitute of Applied Mechanics.* 2008, National Taiwan Unversity: Taipei.
53. The upper limit of the flow rate of side channels is determined by the geometry of crossed channels.
54. L.-L. Yang, H.-Y.Lee., M.-K. Wang, W.-Y. Lin, K.-H. Hsu, Y.-R. Chang, W. Fann, J.D. White, Re*al-time data acquisition incorporating high-speed software correlator for single-molecule spectroscopy. J*ournal of Microscopy, 2009. **234** (9): p. 302-310.
55. Harry, L., III, Th*ioflavine T interaction with synthetic Alzheimer's disease β-amyloid peptides: Detection of amyloid aggregation in solution. P*rotein Science, 1993. 2(**3**): p. 404-410.
56. Voropai, E.S., et al., Sp*ectral Properties of Thioflavin T and Its Complexes with Amyloid Fibrils. J*ournal of Applied Spectroscopy, 2003. **70** (6): p. 868-874.
57. Evan S.-H. Chang, T.-Y.L., Tsong-shin Lim, Wunshain Fann, and Rita P.-Y. Chen, A *new amyloid-like B-aggregate with amyloid characteristics, except fibril morphology. J*ournal of Molecular Biology, 2009. **385:** p. 1257-1265.
58. Nettels, D., et al., Ul*trafast dynamics of protein collapse from single-molecule photon statistics. P*roceedings of the National Academy of Sciences of the United States of America, 2007. **104** (8): p. 2655-2660.
59. Nettels, D., A. Hoffmann, and B. Schuler, Un*folded Protein and Peptide Dynamics Investigated with Single-Molecule FRET and Correlation Spectroscopy from Picoseconds to Seconds. P*roceedings of the National Academy of Sciences of the United States of America, 2008. **112** (19): p. 6137-6146.
60. This simulation is done by Dr. T.S. Lim in Physics Department, Tunghai University, Taichung, Taiwan.
61. Briggs, M.S. and H. Roder, Ea*rly Hydrogen-Bonding Events in the Folding Reaction of Ubiquitin. B*iophysical Journal, 1992. **89** (6): p. 2017-2021.

62. Anfinsen, C.B., Pr*inciples that govern the folding of protein chains. S*cience 1973. **181:** p. 223-229.
63. R. E. Lenkinski, D.M.C., J. D. Glickson and G. Goldstein, Biochim. Biophys. Acta, 1977. **494:** p. 126-130.
64. Makhatadze, G.I., et al., An*ion binding to the ubiquitin molecule. P*rotein Science, 1998. **7** (3): p. 689-697.
65. Ibarra-Molero, B., et al., Th*ermal versus Guanidine-Induced Unfolding of Ubiquitin. An Analysis in Terms of the Contributions from Charge-Charge Interactions to Protein Stability. B*iochemistry, 1999. **38** (25): p. 8138-8149.
66. Khorasanizadeh, S., I.D. Peters, and H. Roder, Ev*idence for a three-state model of protein folding from kinetic analysis of ubiquitin variants with altered core residues. N*at Struct Mol Biol, 1996. **3** (2): p. 193-205.
67. Sosnick, T.R., R.S. Dothager, and B.A. Krantz, Di*fferences in the folding transition state of ubiquitin indicated by Φ and Ψ analyses. P*roceedings of the National Academy of Sciences of the United States of America, 2004. **101** (50): p. 17377-17382.
68. Went, H.M. and S.E. Jackson, Ub*iquitin folds through a highly polarized transition state. P*rotein Engineering, Design & Selection, 2005. **18**(5): p. 229-237.
69. Jackson, S.E., Ub*iquitin : a small protein folding paradigm. O*rganic & Biomolecular Chemistry, 2006. **4**: p. 9.
70. Loladze, V.V. and G.I. Makhatadze, Re*moval of surface charge-charge interactions from ubiquitin leaves the protein folded and very stable. P*rotein Science, 2002. **11** (1): p. 174-177.
71. Hochstrasser, M., L*ingering mysteries of ubiquitin-chain assembly. C*ell, 2006. **124:** p. 27-34.
72. Hershko A, C.A., Th*e ubiquitin system An*nu Rev Biochem, 1998. **67:** p. 425-479.
73. Ciechanover, A., Th*e ubiquitin–proteasome pathway: on protein death and cell life. T*he EMBO Jornal, 1998. **17:** p. 7151
74. Hochstrasser, M., Ub*iquitin signalling: what's in a chain?*, *N*ature Cell Biology, 2004. **6**: p. 571-572
75. Ratner, V., et al., A *general strategy for site-specific double labeling of globular proteins for kinetic FRET studies. B*ioconjug. Chem., 2002. **13** (5): p. 1163-70.
76. Jacob, M.H., et al., Pr*edicting Reactivities of Protein Surface Cysteines as Part of a Strategy for Selective Multiple Labeling. B*iochemistry, 2005. **44** (42): p. 13664-13672.
77. Kao, M.W.-P., et al., St*rategy for Efficient Site-Specific FRET-Dye Labeling of Ubiquitin. B*ioconjugate Chemistry, 2008. **19** (6): p. 1124-1126.
78. We divide all the molecules into three main categories. One is donor-only protein; another is acceptor-photobleaching one, and the other stands for those revealing conformational dynamics.
79. The case of acceptor photobleaching will result into a FRET histogram centering at E = 0 % and 95 % respectively. "Switching" is different from this case.
80. Kao, M.W.-P., et al., St*rategy for Efficient Site-Specific FRET-Dye Labeling of Ubiquitin. 2*008. **19** (6): p. 1124-1126.
81. The bin size of FRET histogram is 2.5 %.
82. Werner, J.H., et al., In*creasing the Resolution of Single Pair Fluorescence Resonance Energy Transfer Measurements in Solution via Molecular Cytometry. A*nalytical Chemistry, 2007. **79** (9): p. 3509-3513.

83. The equation is valid under tha assumption that donor and acceptor are governed by Poisson statistics.
84. Jager, M., E. Nir, and S. Weiss, Si*te-specific labeling of proteins for single-molecule FRET by combining chemical and enzymatic modification. P*rotein Science, 2006. **15** (3): p. 640-646.
85. Kim, P.S. and R.L. Baldwin, Sp*ecific Intermediates in the Folding Reactions of Small Proteins and the Mechanism of Protein Folding. A*nnual Reviews, 1982. **51** (1): p. 459-489.
86. Kim, P.S. and R.L. Baldwin, In*termediates in the Folding Reactions of Small Proteins. A*nnual Reviews, 1990. **59** (1): p. 631-660.
87. Kapanidis, A.N. and S. Weiss, Fl*uorescent probes and bioconjugation chemistries for single-molecule fluorescence analysis of biomolecules. J*ournal of Chemical Physics, 2002. **117** (24): p. 10953-10964.
88. Benjamin, S., Si*ngle-Molecule Fluorescence Spectroscopy of Protein Folding. C*hem Phys Chem, 2005. **6**(7): p. 1206-1220.
89. Hamadani, K.M. and S. Weiss, No*nequilibrium Single Molecule Protein Folding in a Coaxial Mixer. B*iophysical Journal, 2008. **95** (1): p. 352-365.
90. Johnson, C.K., et al., Si*ngle-Molecule Fluorescence Spectroscopy: New Probes of Protein Function and Dynamics.* 2005. p. 10-14.
91. Bilsel, O. and C.R. Matthews, Mo*lecular dimensions and their distributions in early folding intermediates. C*urrent Opinion in Structural Biology, 2006. **16** (1): p. 86-93.
92. Eliezer, D., Bi*ophysical characterization of intrinsically disordered proteins. C*urrent Opinion in Structural Biology, 2009. **19** (1): p. 23-30.
93. Lionel Costenaro, J.G.G., Christine Ebel, and Anthony Maxwell, Sm*all-Angle X-Ray Scattering Reveals the Solution Structure of the Full-Length DNA Gyrase A Subunit. S*tructure, 2005. **13** (2): p. 287-296.